



Citation for published version:

Senthil, K, Pelecanos, L, Rupali, S, Sharma, R & Manish, K 2024, 'Experimental and numerical investigation on soft soil tunnels under impact loading condition', *Journal of Vibration Engineering & Technologies*, vol. 12, pp. 2175-2203. <https://doi.org/10.1007/s42417-023-00973-x>

DOI:

[10.1007/s42417-023-00973-x](https://doi.org/10.1007/s42417-023-00973-x)

Publication date:

2024

Document Version

Peer reviewed version

[Link to publication](#)

Publisher Rights

Other

This is a post-peer-review, pre-copyedit version of an article published in *Journal of Vibration Engineering & Technologies*. The final authenticated version is available online at: <https://doi.org/10.1007/s42417-023-00973-x>

University of Bath

Alternative formats

If you require this document in an alternative format, please contact:
openaccess@bath.ac.uk

General rights

Copyright and moral rights for the publications made accessible in the public portal are retained by the authors and/or other copyright owners and it is a condition of accessing publications that users recognise and abide by the legal requirements associated with these rights.

Take down policy

If you believe that this document breaches copyright please contact us providing details, and we will remove access to the work immediately and investigate your claim.

Journal of Vibration Engineering & Technologies

Experimental and numerical investigation on soft soil tunnels under impact loading condition

--Manuscript Draft--

Manuscript Number:	JVET-D-22-01244R2	
Full Title:	Experimental and numerical investigation on soft soil tunnels under impact loading condition	
Article Type:	Original Paper	
Funding Information:	Royal Society (IES\R2\181054)	Dr Loizos Pelecanos
Abstract:	<p>The tunnels extend the use of underground space for special applications such as transportation, mine development and civil defense. These structures could become susceptible to severe dynamic loads such as traffic loads, pile driving, impact and blast loads. In this context, the experiment and simulations were conducted on semi-cylindrical tunnels of dimensions 1.2 m length × Ø 0.5 m center-to-center and 0.05 m lining thickness under impact loading. The drop height was kept at 3.0 m and the burial depths of the soil cushion were varied as 0, 0.05, 0.10 and 0.15 m to study the effect of the cushion layer under repeated impact load. The experimental results were obtained in terms of damage to the tunnel and displacements in the tunnel under repeated impacts. It was observed that the impact resistance of tunnels increased significantly when the natural burial depth increased from 0.05 to 0.10 m. It was concluded that the tunnel with 0.15 m burial depth was able to resist up to nine impacts as compared to the tunnel without cushion which offered resistance against two impact only. The numerical investigations were performed for each tunnel under repeated impacts using ABAQUS/Explicit. The numerical results were found to be in good agreement with the experimental results in terms of strain in rebar and mid displacement. The parametric study was performed for the influence of mass and velocity of the impactor in terms of crack pattern, impact force, displacement, and energy absorption capacity in the tunnel. On increasing the mass of the impactor from 150 (4.41 kJ) to 400 kg (11.77 kJ), the energy absorption capacity was found to increase from 7.8% to 48.7%, however, on increasing the height of drop from 5 (5.1 kJ) to 20 m (20.40 kJ), the energy absorption capacity of the tunnel was increased from 8.1 to 48.6%. It was concluded that under the low-velocity impact, energy absorption in the tunnel is more sensitive to the mass of the impactor as compared to drop height. It was observed that Yang Qixin's algorithm was the best predicting algorithm among others when comparing peak impact force with the numerical result.</p>	
Manuscript Classifications:	40: Structural vibration, Bridges; 70: Computational methods, FEM, BEM; 130: Vibration mitigation, control; 170: Waves in solids and fluids	
Corresponding Author:	Senthil Kasilingam, Ph. D NIT Jalandhar: Dr BR Ambedkar National Institute of Technology Jalandhar, Punjab INDIA	
Corresponding Author Secondary Information:		
Corresponding Author's Institution:	NIT Jalandhar: Dr BR Ambedkar National Institute of Technology	
Corresponding Author's Secondary Institution:		
First Author:	Senthil Kasilingam, Ph. D	
First Author Secondary Information:		
Order of Authors:	Senthil Kasilingam, Ph. D	
	Loizos Pelecanos, Ph. D	
	Rupali Senthil, Ph. D	
	Rachit Sharma, M. Tech	

	Manish Kumar, M. Tech
Order of Authors Secondary Information:	
Author Comments:	<p>Dear Sir,</p> <p>We are submitting our revised manuscript entitled “Experimental and numerical investigation on soft soil tunnels under impact loading condition” for possible publication in the Journal of Vibration Engineering and Technology.</p> <p>The manuscript addresses a comprehensive experimental and numerical investigation on the influence of cushions on the reinforced concrete semi-cylindrical tunnels under low velocity repeated loading. The impact resistance of tunnel was increased significantly when the burial depth was increased from 0.05 to 0.10 m. The tunnel with 0.15 m burial depth was able to resist up to nine hits as compared to tunnel without burial which offered resistance against two hits only. The influence of mass and velocity of impactor was studied in terms of crack pattern, impact force, displacement and energy absorption capacity in the tunnel. On increasing the energy of impactor from 4.41 kJ to 11.77 kJ, the energy absorption capacity was found increased from 7.8% to 48.7%, however on increasing the height of drop from 5 to 20 m, the energy absorption capacity of tunnel was increased from 8.1 to 48.6%. The energy absorption in tunnel is more sensitive to mass of impactor as compared to drop height. The results obtained have been carefully discussed with respect to the possible reasons behind the findings. The manuscript is based on an original research work carried out by the authors which has neither been published nor is in communication with any other journal.</p> <p>Thanking you Yours sincerely Senthil Kasilingam Assistant Professor Department of Civil Engineering NIT Jalandhar Punjab India</p>
Response to Reviewers:	<p>Author is highly thankful to the reviewer for spending their valuable time on the manuscript and providing constructive suggestion again which led to a significant improvement in the manuscript. The query of the reviewer have been duly incorporated and highlighted by red colour and the response against the reviewer query has been provided below.</p> <p>Reviewer 1#: Query 1: It is surprising that the authors considered their tests as centrifuge tests. From Fig. 2, one can see that the authors conducted reduced-scale model tests only. However, these tests are not carried out under elevated acceleration at all. Please read more technical papers to understand how elevated acceleration can change the stress field in the soil, and reproduce the prototype-scale behavior through centrifuge testing (increased g). Therefore, the use of similitude laws in this investigation can be heavily questioned, since all tests were under the normal ambient condition with 1g, and scaling up may not be trustable. Please further address the testing results properly, before the readers can believe these experimental measurements. Response: Authors have referred to technical papers and the mistake “centrifuge model” was deleted in the revised manuscript, see Section 2.1. As the centrifuge model describes the stresses due to self-weight of the soil which is not considered in the present study. Authors have performed the reduced scale model test considering 0.10, 0.15 and 0.20 m soil cushion. The scaling up for the mass of soil cushion which acts over the tunnel was not considered in the present study due to the insignificant mass of soil. Therefore, the statement “Centrifuge modelling” was deleted from the manuscript since all the tests were performed under the normal ambient condition with 1g without applying any scaling to the soil cushion layer. The law of similitude was applied only for the impact loading cause during the natural phenomenon of rockfall event. The authors were further refined about testing results and the experimental measurements as much as possible in the manuscript, see Section 4.</p>

33 **Keywords:** Reinforced concrete tunnels; Soil cushion; Impact load; Experiment; FE
34 simulations.

1
2 35 **1. Introduction**

3
4 36 The urban population is increasing at a steady pace and often leads to restricted and
5 37 congested spaces. The resolution of constant conflict between the demand for infrastructures
6
7 38 and the supply of residential spaces has often led to the idea of considering an ostensibly hidden
8
9 39 means i.e., the underground space [1]. A tunnel is a superficial underground space that offers
10
11 40 special applications such as transportation, mine development and civil defense. The
12
13 41 construction and operation of the tunnel impose certain risks on all indirectly and directly
14
15 42 involved parties in the project [2]. The underground structures are less vulnerable to seismic
16
17 43 activities [3]. However, these structures become susceptible to severe dynamic loads such as
18
19 44 traffic loads, pile driving, impact and blast loads. Regardless of the variations experienced by
20
21 45 the structure under these dynamic loads, the elastic waves are the main transmitter of energies
22
23 46 that cause vibrations in the system. Thus, it can be inferred that ground vibration mitigations
24
25 47 are similar for each vibration source.

26
27 48 Tunnels are characterized as shallow tunnels which are on ground level and deep tunnels
28
29 49 which are buried deep in the ground. Under static conditions, the shallow tunnels are subjected
30
31 50 to overburden pressure from soil, in situ stresses and seepage of water. Soil pressure act as an
32
33 51 external factor that controls the final failure and deformation behavior of concrete tunnels [4].
34
35 52 The dominant failure modes of reinforcing tunnels under static loading are structural failure
36
37 53 due to plastic rotation of softening hinges, tensile failure caused by localized cracking and
38
39 54 material failure due to concrete deterioration [5]. The tensile and compressive failure can occur
40
41 55 in tunnel crown segments, and it was observed that maximum crown settlement can reach a
42
43 56 rate of increase about 28%. It was suggested to provide local thickening of the support structure
44
45 57 near tunnel interactions in order to improve the stability of tunnels [6,7]. The circular shape of
46
47 58 the tunnels is preferred in case of weak/soft ground due to their own ability to readjust during
48
49 59 the subsequent load changes [8]. The underground structures not only endure static loads but
50
51 60 also dynamic loads due to man-made or natural disasters. The impact or blast loading causes
52
53 61 damage to the underground tunnel running beneath and affects the transportation system and
54
55 62 human lives [9].

56
57 63 Under dynamic conditions, the tunnel influenced by the seismic, impact, or blast loading.
58
59 64 The underground tunnels suffer less damage than surface structures under dynamic conditions.
60
61 65 It was reported that the damage in the tunnel decreases with increasing over- burden depth.
62
63 66 Deep tunnels seem to be safer and less vulnerable to earthquake shaking than shallow tunnels
64
65 67 [10]. Another factor is that tunnels constructed in soil are expected to have more damage

68 compared to openings constructed in competent rocks. Under dynamic conditions, several
69 types of damage were observed, including lining cracks, portal failures, spalling of the concrete
70 lining, groundwater inrush, exposed and buckled reinforcement, displaced lining, rockfalls in
71 unlined sections, lining collapses caused by slope failures, pavement cracks and lining shear-
72 off [11].

73 Rockfall is the primary cause of impact loading on reinforced concrete (RC) tunnels.
74 These impacts have been extensively studied using large scale field test [12] as well as
75 laboratory tests [13,14]. The different mechanisms such as shear as well as the flexural failure
76 of the structural elements were observed under impact load and provided a valuable database
77 for the numerical analysis. It was observed that the deformation of the structure, the weight of
78 the rock and the height of the rockfall were found to have a clear linear relationship. The
79 inclination of slopes at the tunneling threshold often leads to the destabilization of rock faults
80 which can induce serious damage to the tunnel structure.

81 The impact on reinforced concrete structures is often characterized as compression waves
82 at the front side and strong tensile waves at the distal side. The impact on reinforced concrete
83 tunnels is often studied on prototype models. **Dhamne et al.** [15] carried out physical
84 modelling of D-Shaped shallow tunnels to understand tunnel behaviour subjected to a high rate
85 of impact loading (projectile). The deformations obtained in the prototype at the tunnel's crown
86 are 100 times greater than those obtained in the scaled model. The impact energy, which is 105
87 times larger than the scaled model, is the reason for the increased magnitude of displacement.
88 **Gahoi et al.** [16] investigated the deformation behavior of tunnels in rock subjected to impact
89 loading. Important factors governing fracture and deformations in structural integrity were
90 studied under the effect of cover depth and impact energy on shallow tunnel settlement. The
91 reaction of the rock tunnel portal under impact loading, according to **Zaid, et al.** [17]
92 investigated the reaction of the rock tunnel portal under impact loading by varying overburden
93 depth, impact energy and rock weathering grade. It was observed that the deformation behavior
94 was found to be the same for overburden depth and rock weathering grade. **Rao et al.** [18]
95 studied the effect of impact loading developed on shallow tunnels, due to projectile penetration.
96 The probability of projectile penetration within the tunnel lining was observed to decrease as
97 the tunnel's burial depth increased. **Meng et al.** [19] investigated the composite effect of steel
98 fiber and rebar on full-scale steel fiber-reinforced concrete (SFRC) precast tunnel segments.
99 The combined effect of steel fiber and steel rebar found increased load-carrying capacity by
100 increasing the limit of proportionality and delaying the initial crack. **Yan et al.** [20] studied
101 transient analysis of train-to-tunnel impact force using several parameters. The parametric
102 investigation demonstrates that when the impact velocity rise, the dynamic response increases.

103 Major tensile damage was also found in the impact zone, whereas compression damage was
104 observed on the front, distal face of the damaged region. **Sharma et al.** [21] found that the
105 tunnels having the lowest cover depth experience excessive deformation subjected to impact
106 loading. **Wang et al.** [22] performed an experiment on intact and hollow sandstone against
107 various confined pressure under dynamic compressive tests. In comparison to intact sandstone,
108 the hollow cylindrical sandstone experienced lower dynamic strength and a significant critical
109 strain. **Wang et al.** [23] developed a peridynamic model for reinforced concrete shed structures
110 under rockfall impact. It was suggested that simplifying the impact force as the static load is
111 not sufficient to understand the resistance of rock sheds under rock fall.

112 Various mitigation strategies were proposed to evaluate the structural resistance of
113 tunnels. The active and passive open trench was used to control the vibrations [24]. It was also
114 concluded that a larger trench was required at greater distances from the source to accomplish
115 a given amplitude reduction. **Abdul Quadir Bhatti** [25] constructed a three-layer Absorbent
116 System (TLAS) and established a logical impact-resistant modelling methodology for arch-
117 type shelters using the 3-D elastoplastic Finite Element Model (FEM) to compute the maximum
118 input energy for obtaining the end state. When TLAS was used as an absorption system, the
119 transmitted impact force was reduced by half and the displacement at the pithead section was
120 reduced by 75% at the crown, indicating that the RC arch tunnel's impact-resistant ability could
121 be improved. **Volkwein et al.** [26] studied the use of a cushion layer to protect tunnels from
122 impact loading since it is capable of dispersing impact energy and contact pressure to a large
123 extent. **Rezagholilou and Nikraz** [27] observed that when the cushion layer thickness
124 increases, the amount of the impact load reduces. **Baziar et al.** [28] conducted centrifuge
125 experiments to investigate the impact-generated blast loading protection provided by geofam
126 barriers placed between the impact source and underground structures. The efficiency of such
127 barriers against impact loading was found to be significant. **Zaid et al.** [29] used the finite
128 element method to study the effects of impact loads on rock tunnels constructed in different
129 regions in terms of unconfined compressive strength (UCS). The UCS of rock mass plays an
130 important role in the stability of rock tunnels subjected to impact loading from falling rocks or
131 other objects. The absolute value of the touch pressure was significantly reduced when the
132 overlaying sand layer was used, according to **Xu et al.** [30] showing that the sand surface plays
133 a significant role in minimizing the impact force. Layers of gravel can be used as a cushion for
134 structures subjected to rockfalls. Based on probabilistic engineering, the gravel layer shall be
135 used as an energy-absorbent element for rockfall protection [31].

136 Based on the detailed literature review, it was observed that rock fall is the major cause
137 of dynamic damage to the tunnel structures which needs in-depth evaluation. It was assessed

138 that several mitigation strategies have been proposed in the earlier studies to resist the damage
139 inflicted on the structures under dynamic loads. Nevertheless, the transient dynamic response
140 of loose soil as a cushion layer for tunnel structures is an area of interest. Therefore, the current
141 investigation is focussed on the reinforced concrete tunnels under low-velocity impact with
142 and without the use of loose soil as a cushion. The numerical methods are then applied to
143 validate and further study the effect of mass and impact energy on the resistance capability of
144 the tunnel. **Section 2** highlights the experimental investigation along with sample preparation
145 and free-falling drop weight test setup. **Section 3** discussed the constitutive and numerical
146 modelling for different constituting materials using ABAQUS/CAE. **Section 4** highlights the
147 validation and comparison of experimental and numerical investigations under repeated impact
148 load. **Section 5** highlights the energy absorption capacity and deformation of soil under various
149 burial depths of the tunnel. The parametric investigations involving the mass and impact energy
150 of the impactor are highlighted in **Section 6**.

2. Experimental Investigation and Analytical Calculation Methods

The experimental tests were conducted under low velocity drop impact of hemispherical shape for burial depths varying from 0 to 0.15 m. The details of the test instrument and test procedure are explained in detail in this section.

2.1 Experimental Program

The experiments were conducted on a semi-cylindrical tunnel with 1.2 m length \times \emptyset 0.5 m center-to-center and 0.05 m lining thickness to investigate the behavior of the tunnel to low-velocity impact under laboratory-scaled conditions. A semi-circular shape is the most commonly used modern underground structure [32], due to the conservative shape and lesser deformations in the RC tunnel. Also, the law of similitude has been applied to the impact force generated in the model in order to achieve the comparable force in the model to the actual field condition. The scaling up through the law of similitude for the mass of soil cushion which acts over the tunnel was not considered in the present study due to the insignificant mass of soil. The scale factor for different physical-mechanical parameters such as length, velocity, time, energy, acceleration, mass, strain, stress, elastic modulus, and force available in the open source is shown in **Table 1**, which was drawn by [29]. Since the exact similarity of dynamic force is not feasible in the model, the most effective method for matching the model to the prototype is to feature certain similarities and subside others [33]. The similarity criterion used in this study follows the dynamic scale factor in linear elasticity such that, $C_E = C_\epsilon = C_\sigma = 1$, where C_E is the scale factor of elastic modulus, C_ϵ is the scale factor of strain, and C_σ is the scale factor of stress [34]. Using the above criteria, the energy was related to δ^4 for scaling the model to prototype as per [35]. All the tests were performed under the normal ambient condition with

173 **1g without applying any scaling to the soil cushion layer and/or without considering the scaling**
174 **of geostatic stresses of the soil.** In general, the kinetic energies generated in the typical rockfall
175 range up to 5000 kJ with a peak run-on distance of 18 m [36]. Also, the rockfall block velocities
176 range from 30 to 40 m/s with a block mass of about 10 to 20 tons [37]. To develop 5000 kJ
177 impact energy, the mass 104 kg impacted at a velocity of 9.81 m/s along with the scale factor
178 $\delta = 6$ is relevant to cover 90% of rockfall impact events in practical projects. In the present
179 study, the velocity considered in the model covers the practical rockfall event which is
180 equivalent to 4000 kJ ($(mv^2/2) \delta^4 = 104 \times 7.67^2 \times 0.5 \times 6^4$) with an impact velocity of 7.67 m/s
181 due to 3 m free fall drop height ($\sqrt{2gh} = \sqrt{2 \times 9.81 \times 3} = 7.67$ m/s). Therefore, the scale factor
182 $\delta = 6$ was selected as the controlled variable for the experimental program.

2.2 Specimen Preparation

184 The RC tunnel was constructed using M25 ($f_{ck} = 25$ MPa) concrete grade and \varnothing 6 mm
185 for longitudinal as well as lateral reinforcement. The concrete mix design was as per the
186 recommendations of **IS:10262(2019)** [38]. The tunnel was designed as per **IS:456(2000)** [39]
187 and the rebars were placed at 60 mm center-to-center for a reinforcement percentage of 0.4%
188 as shown in **Fig. 1(a)**. The strain gauge, as illustrated in **Fig. 1(b)** was used to determine the
189 strain in rebar for case T-1-BD0. Typical 120-ohm resistance strain gauge with a 10 mm gauge
190 length and located at 0.6 m from the tunnel face, see **Fig. 1(c)**. Strain gauges were glued using
191 cyanoacrylate (CN-Y) adhesives (post-yield). The data was recorded using a high-speed data
192 acquisition system at a rated frequency of 50 kHz.

2.3 Test Setup

194 A typical image of the tunnel with and without a loose soil cushion layer was shown in
195 **Fig. 2(a) and (b)**. The test setup consists of the free-falling impact test machine with a steel
196 wire and a pulley mechanism was developed in the Department of Civil Engineering, NIT
197 Jalandhar, see **Fig. 2**. The drop weight mechanism is supported by an inverted U-frame steel
198 structure that has three numbers of concrete foundation pedestal of RC buried 1.2 m below the
199 ground level and raised approximately 1 m above it. The drop height of weight was kept at 3
200 m for all the cases. The equipment is attached to the concrete using 0.01 m thick base plates
201 (0.203×0.203 m) and 8 foundation bolts with a diameter of 0.012 m that are inserted 0.35 m
202 deep. Using welded connections, four linked steel pipe channels of 3.4 m in height and a
203 diameter of 0.06 m are built on the base plates. Further reinforcement in the form of eight
204 connections spaced by 0.06 m is given between the erected circular rods. To bear the moment
205 created in the construction, steel cross sections are added to the steel beam in the form of lacing
206 and battens, resulting in a monolithic structure. The structure holds two pulleys and a winch

207 that allow the impactor to be raised to a height of 3 m from ground level using a mechanical
208 hoisting mechanism and then free fall to impart impact loading to the specimen.

209 The impactor is made up of three plates measuring $0.25 \times 0.2 \times 0.025$ m that encase a
210 spherical solid steel ball with a diameter of 0.230 m and a hemispherical impactor head
211 assembly, see **Fig. 2(c)**. The hemisphere nose shape impactor has a diameter of \varnothing 0.08 m, and
212 the height of the cylindrical portion is 0.075 m. The weight of the impactor is 104 kg which is
213 dropped from an effective height of 3 meters. Through vast past experimental testing, the
214 efficiency of the system was assumed to be approximately 98%, due to friction in the pulley.
215 The tunnel rests on the soil bed with a specific weight of 1850 kg/m^3 and had no directional or
216 rotational constraints. The experimental campaign for the testing of various tunnels under
217 repeated impact loading is shown in **Table 2**. The designation “T” refers to the tested specimen
218 number and “BD” refers to the Burial Depth of cushioned soil layer used in the experimental
219 testing of tunnels in meters.

220 The crack initiates as the impactor hits the tunnel and the compressive wave propagates
221 at the front face of the tunnel. The cracks are then propagated due to reflective tensile stress
222 waves. As per GB/T 16752-2017 [40], the allowable crack width under static conditions for
223 sewer pipes is 0.2 mm and a length of 300 mm [41]. However, under impact scenarios, the
224 crack widths are generally higher and depend on the strength of the concrete and concrete lining
225 thickness. The limit for crack width for impact scenarios may be taken as (size of aggregate/2.5
226 = $12.5/2.5 = 5$ mm) [42]. Further, in impact loading, the local damage predominates, and the
227 cracks often originate from the location of impact and propagate towards the nearby supports.
228 The width of a crack depends on the damage induced and the intensity of impact, however, the
229 length of the crack is generally formed till the supports or longitudinal to the direction of
230 bending. The direction of bending in a semi-circular-shaped tunnel under point-load impact
231 takes place along the longitudinal direction towards the free end of the support. The failure is
232 characterized as local shear failure due to complete loss of concrete material at the impact zone
233 or the tensile crack width greater than 5 mm.

234 **2.4 Analytical methods for Rockfall impact force**

235 The common calculation methods for peak rockfall impact force are the Swiss method
236 [43], Japanese method [44], Australian method [31], B. S. Guan method [45] and the Method
237 of Tunnel Manual [46]. The Swiss method is developed by Labiouse for rockfall impact force
238 based on rockfall experiments.

$$239 \quad F = 1.765 \cdot M_E^{2/5} R^{1/5} (QH)^{3/5} \quad (1)$$

240 Where M_E is the deformation modulus of the soil cushion layer, Q is the quality of the
241 rockfall, and H is the falling height of the rockfall.

242 Japanese method is based on the Hertz elastic theory, the Japanese road association
 243 presented the relevant semiempirical and semi-theoretical calculation method of rockfall
 244 impact forces.

$$F = 2.108. (Mg)^{2/3} \lambda^{2/5} (H)^{3/5} \quad (2)$$

245 Where g is the gravitational acceleration, λ is the lame constants, and ν is the Poisson's
 246 ratio of soil cushion layer.

247 In 2005, Pichler proposed the Australian method proposed the semiempirical and semi-
 248 theoretical calculation method of rockfall impact force.

$$F = \frac{2Mv_0}{t_w};$$

$$\text{Impact time, } t_w = 2L/v_0 \quad (3)$$

249 Where t_w is the impact time of the rockfall, D is the diameter of the rockfall, M is the
 250 mass of the rockfall and v_0 is the velocity of rockfall.

251 In 1996, B S Guan established the empirical method of impact force based on laboratory
 252 tests. This method considers the influence of the thickness of the soil cushion layer on the
 253 impact force.

$$F = \zeta Ma;$$

$$\text{Acceleration, } a = \frac{\sqrt{2gH}}{t_w} \text{ and}$$

$$\text{Impact time, } t_w = \frac{1}{100} \left[0.097Mg + 2.21h + \frac{0.045}{H} + 1.2 \right] \quad (4)$$

254 Where ζ is the correction coefficient of the rockfall impact force, a is the acceleration
 255 of the rockfall impact, and h is the thickness of the soil cushion layer.

256 The method of tunnel manual refers to an approach recommended in Technical Manual
 257 for Railway Engineering Design Tunnel (Revised Edition), and in essence, it is also an
 258 approximation method of the theorem of momentum.

$$F = \frac{Qv_0}{gt_w};$$

$$\text{Impact time, } t_w = 2h/c;$$

$$\text{Compression wave velocity, } c = \sqrt{\frac{(1-\nu)}{(1+\nu)(1-2\nu)} \cdot \frac{E}{\rho_0}} \quad (5)$$

259 Where c is the reciprocating velocity of compression waves in the soil cushion layer, E
 260 is the modulus of elasticity of the soil cushion layer, ν as Poisson's ratio and ρ_0 is the density
 261 before the deformation of the spherical cavity microbody.

272 3. Constitutive Material Behavior and Numerical Modelling

273 The material model for the concrete, steel rebar and soil were defined using concrete
274 damage plasticity, Johnson-Cook and Drucker Prager model respectively using ABAQUS
275 finite element software is discussed in this section. Detailed numerical modelling was also
276 discussed in this section.

277 3.1 Concrete Damage Plasticity (CDP) Model for Concrete

278 The CDP model uses the concept of isotropic damaged elasticity combined with isotropic
279 tensile and compressive plasticity to represent the inelastic behavior of concrete. This model
280 allows the definition of strain hardening in compression and can be defined as sensitive to strain
281 rate, thus resembling the impact phenomenon more realistically. The model was developed by
282 **Lubliner et al.** [47] and, later modified by **Lee and Fenves** [48] for dynamic and cyclic loading
283 and adopted in ABAQUS/EXPLICIT.

284 The CDP model can be defined in terms of stress-strain response as:

$$285 \sigma_t = (1 - d_t)D_0^{el}: (\varepsilon - \varepsilon_t^{el}) \quad (6)$$

$$286 \sigma_c = (1 - d_c)D_0^{el}: (\varepsilon - \varepsilon_c^{el}) \quad (7)$$

287 Where t is tension, c is compression, σ is stress vectors, ε^{el} is plastic strains, d is the
288 damage function of plastic strain and D_0^{el} is the initial undamaged elastic modulus.

289 The model is idealized as homogeneous and isotropic due to the simplicity of modelling
290 technique and similar elastic moduli observed in compression and tension stress-strain
291 diagrams. The CDP model considers non-associated plastic flow rules. The non-associative
292 plastic flow rule has been characterized as

$$293 G_p = \sqrt{(\varepsilon\sigma_{t0}\tan\psi)^2 + \left(\frac{3}{2}s:s\right)} - \bar{p}\tan\psi \quad (8)$$

294 Where ψ represent the dilation angle and σ_{t0} as uniaxial tensile stress at failure and ε as
295 eccentricity. The eccentricity parameter, m of the flow potential, ε with a value of 0.1 has been
296 found by comparing the experimental data from bi- and triaxial strength results [48]. The
297 compressive and tensile damage parameters, $D_c(\tilde{\varepsilon}_c^{pl})$ and $D_t(\tilde{\varepsilon}_t^{pl})$ can be characterized using
298 the degraded elastic compressive and tensile stiffness as $(1 - D_c)E_c$ and $(1 - D_t)E_c$
299 respectively, where E_c is modulus of elasticity. The material damage is characterized from zero
300 to one with zero being undamaged and one as completely damaged. The material model
301 parameters used in this study are based on the studies of [49–51] and are shown in **Tables 3**
302 **& 4.**

303 3.2 Johnson-Cook Model for Reinforcement Bar

304 The Johnson-Cook model [52] was used to define the behavior of the ductile materials and is
305 used in the present study to define the strength and fracture behavior possessed by the steel

306 reinforcement bars. The Johnson-Cook model is based on the strain hardening principle and
 307 von-mises yield criteria. The equivalent von Mises yield stress is therefore expressed as;

$$\bar{\sigma} = [A + B(\bar{\epsilon}^{pl})^n] \left[1 + C \ln \left(\frac{\dot{\bar{\epsilon}}}{\dot{\bar{\epsilon}}_0} \right) \right] [1 - \hat{T}^m] \quad (9)$$

309 Where $\bar{\epsilon}^{pl}$ is equivalent plastic strain, A, B, n and m, are material parameters measured
 310 at or below the transition temperature, T_o . There are various constants used to define the
 311 Johnson-Cook model for steel, which comprises yield strength, strain hardening coefficient,
 312 strain hardening exponent, strain rate sensitivity and thermal softening parameter. The
 313 Johnson-Cook material parameters based on the study by **Iqbal et al.** [53] and **Kumar et al.**
 314 [54] were considered for the present study and are tabulated in **Table 5**.

3.3 Drucker Prager Model for Soil

315 Drucker Prager model [55] was used to define the behavior of the soil part. The yield
 316 area in this model consists of two main areas i.e., the fracture area providing the flow cut and
 317 the cover, crossing the equivalent pressure. This model simplified the Mohr-Coulomb model
 318 by substituting the hexagonal-shaped failure cone with a simple failure cone. The Drucker-
 319 Prager hardening behavior is defined by yield stress versus absolute plastic strain values. The
 320 Drucker-Prager can be illustrated as

$$F = \frac{q}{2} \left[1 + \frac{1}{K} - \left(1 - \frac{1}{K} \right) \left(\frac{r}{q} \right)^3 \right] - p' \tan \beta - d = 0 \quad (10)$$

321 Where q is the deviatoric stress tensor, p' is mean stress, K determines the yield surface
 322 shape and maintains its convexity in the deviatoric (π) plane, r is the third deviatoric stress
 323 tensor invariant, β is related to internal friction (ϕ) angle for no dilatancy stage given by

$$\tan \beta = \frac{\sqrt{3} \sin \phi}{\sqrt{1 + \left(\frac{1}{3} \right) \sin^2 \phi}} \quad (11)$$

324 And d is the hardening parameter related to cohesion (c) given by

$$\frac{d}{c} = \frac{\sqrt{3} \cos \phi}{\sqrt{1 + \left(\frac{1}{3} \right) \sin^2 \phi}} \quad (12)$$

325 The dilation angle calculation is based on the studies of [56,57] and it is preferable to
 326 keep it at 0 degrees. However, the value of the dilation angle is considered as 1° because the
 327 strength and dilatancy rate reduction that takes place in dense soils must be considered when
 328 dealing with problems involving geotechnical stability [58]. The corresponding Drucker Prager
 329 model parameters used in this study are given in **Table 6**.

3.4 Finite Element Modelling

330 Numerical investigations and modelling of the assembly were carried out using
 331 ABAQUS/CAE. A typical assembly for 0.15 m burial depth was shown in **Fig. 3**. The model

337 was based upon the Lagrangian formulation, and the tunnel and buried soil were modeled as
338 three-dimensional deformable bodies as shown in **Fig. 3(b), (c)**. The main and transverse
339 reinforcement was provided with 6 mm diameter bars, placed at a spacing of 0.06 m center to
340 center, in proximity to the experimental condition. The impactor was modelled as an analytical
341 rigid body with a mass inertia of 104 kg was assigned to it as shown in **Fig. 3(d)**. The shape of
342 the impactor was semi-spherical and the contact between various bodies was given using
343 general contact for all exterior surfaces. The tangential contact was given using the Coulomb
344 friction model with a coefficient of friction of 0.30 and normal HARD contact was used. The
345 embedded constraint was used to model the interaction between the concrete and steel rebar.
346 The bottom soil was fixed, and all degrees of freedom were restrained. The burial soil was
347 restrained from motion in the x-direction. The tunnel was restricted in the z-direction and
348 corresponding rotational degrees of freedom were also restricted. The impactor was given an
349 initial velocity of 7.67 m/s. The mesh for 3-D deformable bodies was C3D8R, an 8-noded
350 linear brick element with reduced integration. For reinforcement, a 2-node linear beam in space
351 (B31) element was used. A mesh size of 20 mm was provided for both longitudinal and
352 transverse reinforcement.

353 The sensitivity of the mesh size was studied on tunnel T-1-BD0 against a 3 m drop height.
354 A detailed mesh convergence has been performed to study the effect of mesh size in the
355 concrete corresponding to mesh sizes of 20, 15, 12, 10, 7.5 and 6 mm. The results in terms of
356 the peak tunnel displacement in the downward direction at the point of impact were used for
357 mesh convergence. The peak displacement on the tunnel with 20, 15, 12, 10, 7.5 and 6 mm
358 mesh size was found to be 21, 28, 29, 34 and 33 mm, respectively. The optimum mesh is taken
359 as 7.5 mm based on the mesh convergence study as the computational cost increased by 1.74
360 times for 6 mm mesh as compared to 7.5 mm mesh whereas the variation in displacement is
361 2.9%. Therefore, keeping the computational cost, a mesh size of 7.5 mm is chosen for the
362 numerical simulations. **Fig. 4(a)**. For numerical validation, the predicted micro strain on the
363 tunnel longitudinal reinforcement bar with varying mesh size was compared with the
364 experimental results, see **Fig. 4(b)**. The peak strain was found to be 66, 133, 207, 174 and 196
365 and 231 $\mu\epsilon$ on the tunnel with 20, 15, 12, 10, 7.5 and 6 mm mesh size, respectively whereas
366 the measured peak strain was found to be 169.36 $\mu\epsilon$ which is close to the simulation results of
367 mesh size of 10 mm. However, the peak midpoint displacement was found closer to 7.5 mm
368 i.e., 34 mm rather than 10 mm mesh size i.e., 29 mm as compared to experimental results i.e.,
369 32 mm. The difference in results could be attributed to the absence of strain rate consideration
370 in the model. Further, the compressive fracture energy of concrete is not taken into account
371 concerning the change in mesh size.

372 4. Comparison of Experimental and Numerical Results

373 The damage pattern on all four tunnels observed from the experiment was compared with
1 374 the numerical simulations. The resistance offered by the tunnels with different burial depth
2 375 cases against impact loading of 3 m drop height was compared. The compression, as well as
3 376 tension damage in the tunnel, was quantified and the damage mechanism involved in the
4 377 dynamic event was discussed.

378 4.1 Comparison of tunnel T-1-BD0

379 The tunnel T-1-BD0 was studied under a 3 m drop height and the sample resisted up to
11 380 two impacts until complete concrete failure at the impacted location. For the first impact, the
12 381 tunnel experiences a frontal crater with a longitudinal crack, see Fig. 5(a). The rear face
13 382 experiences longitudinal flexural cracks with an average width of 2.5 mm, see Fig. 5(b). Lateral
14 383 cracks were experienced for the side face where the maximum crack width was 2 mm, see Fig.
15 384 5(c). The average diameter of the crater was 40 mm, see Fig. 5(d). The scabbing and spalling
16 385 phenomenon was observed for both the rear and front faces respectively. The major failure of
17 386 the tunnel was a flexural failure due to tensile waves at the rear face. The same can be observed
18 387 for tensile and compression damage in the numerical study, see Fig. 6(a-i)-(b-ii). For the
19 388 second impact, major damage occurred to both front as well as rear faces. For the front face,
20 389 the crater diameter expanded to 80 mm and major longitudinal damage was observed, see Fig.
21 390 5(e). For the rear face, the major failure was punching shear at the location of impact along
22 391 with a flexural crack, see Fig. 5(f). The scabbing observed at the rear face has an average
23 392 diameter of 260 mm. The tunnel completely failed at the point of impact and one major crack
24 393 propagated longitudinally along both faces and further enlarged the cracks at the side faces.
25 394 The punching shear failure occurs at a shear angle of 32° indicating severe damage to the rear
26 395 face of the tunnel. The same was observed for numerical simulation where severe compression
27 396 damage to the front face along with longitudinal tensile damage at the rear face was observed,
28 397 see Fig. 6(a-iii)-(b-iv). The radial damage was equivalent for both the faces in numerical
29 398 simulation, see Fig. 6(a-v) & (b-v). The peak deformation in rebar was 30 mm and 51.2 mm
30 399 corresponding to the first and second impacts. It was observed that the deformation in concrete
31 400 was well above the complete damage state which was obvious from the deformation in rebar.

401 4.2 Comparison of tunnel T-2-BD5

402 The tunnel T-2-BD5 was tested under similar loading conditions for a soil cushion layer
403 thickness of 0.05 m. The tunnel was able to take three impacts before complete failure. During
404 the first impact, the impactor completely perforated the soil cushion layer and impacted the
405 tunnel. The damage to the tunnel was visible in the form of the side face radial cracks of width
406 1-2 mm, see Fig. 7(a). The damage to the rear face of the tunnel experiences a longitudinal

407 flexural crack that propagated along the whole length of the tunnel, see **Fig. 7(b)**. The width of
408 the cracks was approximately 3 mm. The front face of the tunnel experiences compression
409 damage with crater formation whose diameter is \varnothing 30 mm. The numerical model was able to
410 correctly capture the damage on the tunnel front and rear surface, see **Fig. 8**. It was observed
411 that the compression damage in the tunnel occurred radially at the front face whereas the tensile
412 wave propagated longitudinally at the rear face of the tunnel, see **Fig. 8**. As the number of
413 impacts increases, the width of crack increases, however no change in the length of crack was
414 observed.

415 Under the second impact, the radial cracks get enlarged, see **Fig. 7(c)** and scabbing was
416 observed at the rear face of the tunnel. The longitudinal cracks got wider at the rear face, see
417 **Fig. 7(d)**. The size of the frontal crater was approximately equal to the diameter of the impactor
418 i.e., 75 mm. A similar pattern was observed for numerical results where longitudinal
419 compressive waves induce damage to the front face whereas punching shear failure was formed
420 at the rear face of the tunnel. It was observed that compressive and tensile waves cause
421 similitude of damage at the front and rear face respectively, see **Fig. 8**. From the numerical
422 study, it was evident that the damage to the tunnel occurred as longitudinal flexural cracks as
423 well as punching shear failure. The 0.05 m burial depth was proven to be ineffective for low-
424 velocity impact loading based on the current investigations. In the case of the third impact,
425 severe damage was observed on both sides of the tunnel. The front face has severe spalling and
426 crater formation occurred whose diameter was 80 mm and further concrete was completely
427 eroded from the impact zone, see **Fig. 7(e)**. The rear face of the tunnel experiences severe
428 scabbing of concrete with many flexural crack formations, see **Fig. 7(f)**. The scabbing diameter
429 was approximately equal to 300 mm. The punching shear failure occurs at a shear angle of 27°
430 indicating severe damage to the rear face of the tunnel. The side face experiencing tensile
431 damage in numerical simulations was like an experimental pattern as shown in **Fig. 8**. The
432 downward displacement on the rebar for the first, second and third impact was 26, 39 and 56
433 mm respectively. It was observed that the deformation in concrete was well above the complete
434 damage state which was obvious from the deformation in rebar.

435 **4.3 Comparison of tunnel T-3-BD10**

436 The tunnel T-3-BD10 was tested under similar loading conditions for a soil cushion layer
437 thickness of 0.1 m. **The tunnel sustained eight impacts before complete failure.** From the first
438 to fifth impact, minor side face cracks were formed in the tunnel and the width of the cracks
439 formed was increased from 1 mm to 3 mm. It was observed that the 10 mm soil cushion layer
440 had a significant effect on the impact resistance under impact loading. The soil layer was able
441 to resist the impact and prevent damage to the tunnel till the fourth impact. There were no side

442 face cracks observed in the T-2-BD10 tunnel till the fifth impact, see **Fig. 9(a)-(d)**. For the fifth
443 impact, the radial cracks with a width of 3 mm were formed, see **Fig. 9(e)**. For the sixth impact,
444 the target was completely perforated the cushion layer of soil at the impact zone and flexural
445 cracks were developed on the rear face and extended to the side face of the tunnel, see **Fig. 9(f-
446 i)-(f-ii)**. A similar damage pattern with enlarged cracks was observed during the seventh
447 impact, see **Fig. 9(h-i)-(h-ii)**. The soil was completely deformed and moved away from the
448 impact zone during the fifth and sixth impacts, see **Fig. 9(g) & (j)**.

449 During eight impacts, severe damage was observed for the tunnel at the front as well as
450 the rear face, see **Fig. 9(k) & (l)**. The impactor was able to fully penetrate the front face where
451 crater formation was observed with a diameter equal to the impactor diameter. Also, the
452 spalling of concrete was observed at the tunnel ends. At the rear face, damage to the tunnel had
453 large scabbing with an average diameter of 280 mm. The punching shear failure occurs at a
454 shear angle of 29° indicating severe damage to the rear face of the tunnel. The numerical
455 simulation was performed till the fourth impact in comparison with the experimental results.
456 The numerical simulation was able to correctly capture the experimental results. However, the
457 damage to the tunnel was overpredicted and it had only four impacts for the tunnel to fail. The
458 radial cracks were correctly captured in the numerical simulation, see **Fig. 10**. The deformation
459 in the tunnel rebar for four impacts increased from 5.3 mm to 53 mm.

460 **4.4 Comparison of tunnel T-4-BD15**

461 The tunnel T-3-BD15 was tested under similar loading conditions for a soil cushion layer
462 thickness of 0.15 m. **The tunnel sustained nine impacts before complete failure.** From the first
463 to sixth impact, minor cracks were formed in the tunnel side face and the width of cracks was
464 found to increase from 1 to 3 mm. It was observed that the 0.15 m soil cushion layer had a
465 significant effect on the impact resistance under impact loading. The soil layer was able to
466 resist the impact and prevent damage to the tunnel till the fifth impact. There were no side face
467 cracks observed in the T-2-BD15 tunnel till the fifth impact. For the fifth impact, the radial
468 cracks with a width of 2 mm formed on the side face, see **Fig. 11(a-i)**. Similarly, rear face
469 cracks were formed whose width is 5 mm, see **Fig. 11(a-ii)**. During the sixth impact, the side
470 face cracks were found enlarged, see **Fig. 11(b-i)**, and further rear face scabbing of concrete
471 was observed, see **Fig. 11(b-ii)**. After the sixth impact, the tunnel damage was quite severe
472 where no cushion layer was available at the impact location to dissipate the energy. The cracks
473 at the side face were found enlarged during the seventh and eighth impact, see **Fig. 11(c-i) &
474 (d-i)** and a large mass of concrete was found scabbed at the rear face, see **Fig. 11(c-ii) & (d-
475 ii)**.

476 During the ninth impact, severe damage was observed to the tunnel at the front as well
477 as the rear face, see **Fig. 11(e) & (f)**. The impactor was able to fully penetrate the front face
478 where crater formation was observed with a diameter equal to the impactor diameter. However,
479 no spalling of concrete was observed at the tunnel ends. **The longitudinal compressive wave**
480 **was the primary cause of flexural failure at the front surface of the tunnel.** The crater diameter
481 at the front face had a diameter of 75 mm. At the rear face, damage to the tunnel had large
482 scabbing with an average diameter of 360 mm. The punching shear failure occurs at a shear
483 angle of 21° indicating severe damage to the rear face of the tunnel. The numerical simulation
484 was performed till the 4th impact in comparison with the experimental results. The numerical
485 simulation was able to correctly capture the experimental results, see **Fig. 12**. The radial cracks
486 were correctly captured in the numerical simulation, see **Fig. 12**. **The deformation in the tunnel**
487 **rebar was found to increase from 5.3 to 53 mm from first to fourth impacts.**

5. Energy Absorption and Deformation on Tunnel using FE Simulations

489 The predicted energy absorption capacity was compared for each cushion layer thickness
490 and further extended numerically to 0.30 m burial depths. The stress in tunnel and deformation
491 that occur in rebar was also studied for varying burial depths and discussed in this Section.
492 Further, the deformation in bed soil was also compared against each burial depth and discussed.

5.1 Energy Absorption Capacity under Repeated Impact Load

494 The load versus displacement response of tunnels under varying burial depths for
495 repeated impacts was presented in **Fig. 13**. The depth of the cushion layer was extended to 0.3
496 m for numerical study. The peak impact force for various burial depth cases under repeated
497 impacts is presented in **Table 7**. The peak impact force for zero burial depth was found to be
498 95.55 kN and the corresponding peak mid-node deformation was 46.48 mm. The calculated
499 impulse and energy absorption capacity of the zero burial depth tunnel was 0.85 kN-s and
500 2998.62 kN-mm respectively, see **Table 7**. During the second impact, the peak impact force
501 increased to 110.38 kN and the peak displacement was 79.34 mm, see **Table 7**. The
502 corresponding impulse and energy absorption capacity was 0.91 kN-s and 2912.05 kN-mm
503 respectively. It was observed that the peak impact force, as well as impulse, was increasing
504 with the second impact whereas energy absorption was similar. The rise in peak impact force
505 with repeated impact was also found because of the contact between the impactor and concrete
506 part and increased values of plastic strains than strain at failure resulting in over elongation of
507 elements [59]. The force-displacement plot for the 0.05 m burial depth case was shown in **Fig.**
508 **13(a)**. For 0.05 m burial depth, the peak impact force and displacement for 1st impact were
509 found to be 204.32 kN and 35.27 mm respectively. For the 2nd and 3rd impact, the peak impact
510 force was increased to 221.41 kN and then reduced to 200.65 kN. The peak displacement for

511 the 2nd and 3rd impact was found to be 56.87 and 73.88 mm corresponding to the initial position.
512 The impulse and energy absorption capacity of 0.05 m burial depth tunnel was found to be
1 513 increasing on repeated impacts, see **Table 7**. For 0.1 m burial depth, the peak impact force for
2 514 1st to 4th impact was 184.34, 184.21, 209.6 and 210.54 kN respectively. It was observed that
3 515 the peak impact force was increasing with each subsequent impact, see **Table 7**. The peak
4 516 displacement for 0.1 m burial depth increased from 13.67 to 68.65 mm, indicating failure of
5 517 concrete at the impacting surface. The load-displacement curve was plotted for 0.1 m burial for
6 518 energy absorption calculations, see **Fig. 13(b)**. The impulse and energy absorption capacity of
7 519 the tunnel was first increased from 1st to 3rd impact and then decreased for 4th impact, see **Table**
8 520 **7**.

16 521 For 0.15 m burial depth, the peak force was reduced to 155.43 kN for 1st impact. For each
17 522 subsequent impact, the peak impact force was comparable to the 0.05 and 0.1 m burial depth
18 523 cases, see **Table 7**. The load-displacement curve for 0.15 m burial depth indicates that much
19 524 of the energy got absorbed into the soil layer, see **Fig. 13(c)**. Therefore, lower energy
20 525 absorption values were found for the 0.15 m burial depth tunnel, see **Table 7**. For 0.2 m tunnel
21 526 depth, there was a considerable drop in peak deformation, however, the peak force was
22 527 comparable to the other cases, see **Table 7**. The energy absorption capacity of the tunnel was
23 528 significantly lower for 0.2 m burial depth due to the lower deformations under repeated
24 529 impacts, see **Fig. 13(d)**. It can be concluded that above a threshold of 0.15 m burial depth, the
25 530 deformations in the tunnel can be significantly lowered. The soil cushion layer above 0.15 m
26 531 was proven to be quite effective in controlling the damage to the tunnel under impact loading.
27 532 For 0.25 m burial depth, the impact force was reduced as compared to earlier cases. The impact
28 533 force for impact 1-4 was found to be 106, 157, 176.06 and 169.06 kN respectively. The peak
29 534 deformations in the tunnel were significantly lower than lower burial depth cases as shown in
30 535 **Fig. 13(e)**. The 0.3 m burial depth observed a lower impact force for 1st impact as compared to
31 536 the lower burial depth, however, the peak force was increased for subsequent impacts and
32 537 comparable to the other cases, see **Table 7**. The force-displacement curve was plotted for the
33 538 energy absorption capacity of the tunnel as shown in **Fig. 13(f)**. It was concluded that above
34 539 0.2 m burial depth the energy absorbed by the tunnel was similar in magnitude as well as
35 540 comparable peak deformations observed. The impulse was found to be comparable for each
36 541 burial depth case. Therefore, it was concluded that the impact duration was similar for each
37 542 burial depth tunnel.

56 543 **5.2 Soil Deformation under Repeated Impact Load**

58 544 The deformation of bed soil under repeated impacts was shown in **Fig. 14**. The
59 545 deformation in the soil was increased with each subsequent impact and is presented in **Table**

546 7. For 5 mm BD the deformation in the bed soil increased to 21 mm for the 3rd impact, see **Fig.**
547 **14**. The deformation in bed soil was propagated longitudinally on the inner surface of the tunnel
548 bed soil. It was observed that the deformation in the inner side of the tunnel bed soil was
549 hogging. The soil was deformed upwards along the periphery of the tunnel due to the natural
550 constrained boundary conditions. The deformation of the 0.10 m BD tunnel was lower for 1st
551 impact as compared to 0.05 m BD, however equal magnitude of deformation was observed
552 below the tunnel lining for subsequent impacts, see **Fig. 14**. Till 0.15 m BD, the deformation
553 in the bed soil was of equal proportions on both sides. The deformation kept on reducing as the
554 depth of the buried soil increased. For burial depths of more than 0.15 m, the deformation
555 primarily occurred on the left side, see **Fig. 14**. The hogging deformation primarily occurred
556 on the soil directly below the tunnel. For BD 0.20 m and higher, the bed soil experiences a
557 similar magnitude of deformation below the tunnel lining, see **Fig. 14**. It can be concluded that
558 the 0.15 m soil cushion layer was most efficient and economical for the application of impact
559 resistance for RC tunnels.

560 **6. Influence of Mass and Velocity of Impactor**

561 To study the influence of mass and impactor velocity on the behavior of underground
562 tunnels, numerical investigations were performed on the tunnel with a constant burial depth of
563 0.15 m. The predicted results are presented in terms of tunnel damage, bed soil deformation
564 and energy absorption capacity under varying the mass and velocity of the impactor.

565 **6.1 Varying Mass of Impactor**

566 The parametric study was performed to evaluate the damage to the tunnel for varying
567 masses of impactor as 150, 200, 300 and 400 kg for 0.15 m soil cushion layer. The impact
568 resistance and energy absorption capacity of the tunnel were evaluated and deformation in bed
569 soil was also studied.

570 The compression and tension damage to the 0.15 m BD tunnel was evaluated of different
571 impactor masses of 150, 200, 300 and 400 kg as shown in **Fig. 15**. On increasing the mass of
572 the impactor, the compression damage to the tunnel increased longitudinally on the front face,
573 see **Fig 15(a-i)-(d-i)**. On the rear face, the compression damage was propagating radially
574 outward from the point of impact, see **Fig 15(a-ii)-(d-ii)**. As the mass of the impactor increased,
575 the damage zone was getting enlarged for compression damage at the rear face of the tunnel. It
576 was observed that 0.15 m BD soil was able to resist the impact till 200 kg impactor mass above
577 which large longitudinal damage was observed. The tension damage was propagating laterally
578 towards the free edges from the point of impact at the front face, see **Fig. 15(a-iii)-(d-iii)**. The
579 damage intensity increased drastically as the mass of the impactor increases from 300 kg above,
580 see **Fig. 15(c-iii)-(d-iii)**. The tension damage to the rear face of the tunnel propagated

581 longitudinally towards the free edge, see **Fig. 15(a-iv)-(d-iv)**. For an impactor mass of 400 kg,
582 the tunnel expanded radially outwards indicating complete failure along the longitudinal plane.

1
2 583 The impact force versus time plot of 0.15 m BD tunnel under a varying mass of impactor
3 584 was shown in **Fig. 16(a)**. It was observed that the peak impact force did not show a clear trend
4
5 585 with the change in impactor mass, however, the time history of the impact force plot for
6
7 586 different cases was similar. The peak impact force for different cases was presented in **Table**
8
9 587 **8**. It was observed that the peak impact force was 308.90 kN for 400 kg mass of impactor
10
11 588 among all other cases. It was concluded that the impact resistance of the 0.15 m BD tunnel was
12
13 589 dependent to a lesser extent on the mass of the impactor where only slight variations in peak
14
15 590 impact force were observed. The displacement in the tunnel for varying mass of impactor was
16
17 591 shown in **Fig. 16(b)**. It was observed that the peak displacement was increasing with the
18
19 592 impactor mass. It was observed that there is an abrupt change in the displacement of the tunnel
20
21 593 after 300 kg impactor mass because the concrete elements below the impact locations were
22
23 594 distorted and extended to larger plastic strains. The use of element erosion algorithms can
24
25 595 ensure that the distorted elements are removed from the simulation. The peak displacement
26
27 596 showed a linear trend with the impact mass as shown in **Table 8**. The peak bed soil deformation
28
29 597 was presented in **Table 8**. It was observed that the peak bed soil deformation was increased
30
31 598 with the increase of impactor mass and there was an abrupt change in the deformation against
32
33 599 300 kg impactor mass. In addition to that, the pattern of deformation from the present study
34
35 600 has been compared with the literature. Similar results were observed by Gahoi et al. [16] and
36
37 601 Zaid [50] as the higher deformations due to the increase of mass of the impactor.

38 602 The impulse was calculated by integrating the impact force time history and presented in
39
40 603 **Table 8**. It was observed that the impulse was increased with an increasing mass of the
41
42 604 impactor. The impulse for the varying impactor mass was increased. The higher impulses
43
44 605 observed were directly dependent on the higher initial impact energy to the system. The energy
45
46 606 absorption capacity of the plate was obtained by extracting the area of the load-displacement
47
48 607 response and the energy absorption capacity of the tunnel for varying masses of the impactor
49
50 608 was presented in **Table 8**. The energy absorption capacity was increased as the mass of the
51
52 609 impactor increased due to higher deformations observed. The increased deformations are
53
54 610 directly related to the energy absorbed and therefore because of the absence of element removal
55
56 611 algorithms, the plastic strains increased rapidly in the concrete.

57 612 The contours of the base soil bed deformation were presented in **Fig. 17**. It was observed
58
59 613 that the negative deformations on the bed soil were mostly constricted to the base of the tunnel
60
61 614 lining. The positive deformations occurred at the base of the tunnel where hogging moments
62
63 615 were observed. The deformation contours were similar in nature for each case as shown in **Fig.**

616 17. The peak positive deformations for 150, 200, 300 and 400 kg were 1.9, 2.4, 4.1 and 5.8 mm
617 as shown in **Fig. 17(a) - (d)**. The peak deformation showed a linear increase with increasing
1 618 the mass of the impactor. The hogging deformations were mostly restricted to a smaller area
2 619 around the edges of the tunnel. The area of hogging deformations increased with the increase
3 620 in the mass of the impactor. The hogging deformations in bed soil below the tunnel were
4 621 constricted to a smaller area as the mass of the impactor was increased, see **Fig. 17(a) – (d)**.
5 622 The peak positive deformations were observed at the mid location below the tunnel because of
6 623 the reflected compressive wave from the tunnel boundaries.

624 6.2 Varying Velocity of Impactor

625 The parametric study for varying impactor velocities of 9.9, 14, 17.15 and 19.81 ms⁻¹
626 corresponding to the height of the impact as 5, 10, 15 and 20 m was studied for compression
627 and tension damage. Also, the impact resistance and energy absorption capacity were studied
628 for varying impactor velocity. Further, the deformation in the soil bed was investigated under
629 varying impactor velocities.

630 The compression and tension damage to the 0.15 m BD tunnel was evaluated at different
631 impactor velocities of 9.9, 14, 17.15 and 19.81 ms⁻¹ as shown in **Fig. 18**. On increasing the
632 velocity of the impactor, the compression damage to the tunnel increased longitudinally on the
633 front face, see **Fig 18(a-i)-(d-i)**. On the rear face, the compression damage was propagating
634 radially outward from the point of impact, see **Fig. Fig 18(a-ii)-(d-ii)**. As the impactor velocity
635 increased, the damage zone was getting enlarged for compression damage at the rear face of
636 the tunnel. It was observed that 0.15 m BD soil was able to resist the impact till 14 m/s impactor
637 mass above which large longitudinal damage was observed. The tension damage was
638 propagating laterally towards the free edges from the point of impact at the front face, see **Fig.**
639 **18(a-iii)-(d-iii)**. The damage intensity was increased drastically as the impactor velocity was
640 above 14 m/s, see **Fig. 18(b-iii)-(d-iii)**. As the impactor velocity increased, the tension damage
641 at the front face started propagating in the longitudinal direction also, see **Fig. 18(d-iii)**. The
642 tension damage to the rear face of the tunnel propagated longitudinally towards the free edge,
643 see **Fig. 18(a-iv)-(d-iv)**. As the impactor velocity increased, the tension damage area along the
644 longitudinal plane increased significantly.

645 The impact force versus time plot of the 0.15 m BD tunnel under the varying velocity of
646 the impactor was shown in **Fig. 19(a)**. It was observed that a similar trend for impact force
647 versus time plot was observed as the impactor velocity increased, however, the plateau peaks
648 were lesser in number for 19.81 ms⁻¹ impact velocity, see **Fig. 19(a)**. The peak impact force for
649 different cases was presented in **Table 9**. It was observed that the peak impact force first
650 decreased as the impactor velocity increased from 9.9 - 14 ms⁻¹ from 235.31 to 189.33 kN and

651 then increased significantly for 17.15 and 19.81 ms⁻¹ at 416 and 630.14 kN respectively. It was
652 concluded that the impact resistance of the 0.15 m BD tunnel was significantly dependent on
1 653 the impactor velocity. The displacement in the tunnel for varying mass of impactor was shown
2
3 654 in **Fig. 19(b)**. The tunnel displacement versus time plot has a similar trend for change in
4
5 655 impactor velocity where the displacement in the tunnel first increased and then residual
6
7 656 deformation was observed. It was observed that the peak displacement was increasing with the
8
9 657 impactor mass, see **Table 9**. The peak displacements for 9.9, 14, 17.15 and 19.81 ms⁻¹ were
10
11 658 8.17, 25.45, 53.88 and 81.59 mm respectively. The peak bed soil deformations for different
12
13 659 cases were presented in **Table 9**. It was observed that the peak bed soil deformation increased
14
15 660 linearly with the impactor velocity.

16 661 The impulse was calculated by integrating the impact force time history and presented in
17
18 662 **Table 9**. It was observed that the impulse was increased with the increasing velocity of the
19
20 663 impactor. The impulse was increased linearly with the impactor velocity. The higher impulses
21
22 664 observed were directly dependent on the higher initial impact energy to the system. The peak
23
24 665 forces were much higher as the velocity of the impactor was increased however the impulses
25
26 666 did not observe such behavior. Therefore, it can be concluded that the plateau of forces was
27
28 667 similar in increasing the velocity of the impactor. The energy absorption capacity of the plate
29
30 668 was obtained by extracting the area of the load-displacement response and the energy
31
32 669 absorption capacity of the tunnel for the varying velocity of the impactor was presented in
33
34 670 **Table 9**. The energy absorption capacity increased significantly as the velocity of the impactor
35
36 671 increased due to higher impact forces and deformations observed. The energy absorption
37
38 672 capacity was related to both peak force and displacement with impactor velocity and the
39
40 673 corresponding values of energy absorption capacity for 9.9, 14, 17.15 and 19.81 ms⁻¹ were
41
42 674 414.10, 2172.16, 5372.27 and 9922.37 kN-mm respectively.

43 675 The contours of the base soil bed deformation were presented in **Fig. 20**. It was observed
44
45 676 that the negative deformations on the bed soil were mostly constricted to the base of the tunnel
46
47 677 lining. The positive deformations occurred at the base of the tunnel where hogging moments
48
49 678 were observed. The deformation contours were similar in nature for each case as shown in **Fig.**
50
51 679 **20**. The peak positive deformation for 9.9, 14, 17.15 and 19.81 ms⁻¹ were 2, 4.8, 6.6 and 7.4
52
53 680 mm as shown in **Fig. 20(a) - (d)**. The peak deformation showed a linear increase with
54
55 681 increasing the impactor velocity from 2.0 to 7.4 mm. The hogging deformations were mostly
56
57 682 restricted to a smaller area around the edges of the tunnel. The area of hogging deformations
58
59 683 increased with the increase in the velocity of the impactor, see **Fig. 20(d)**. The hogging
60
61 684 deformations in bed soil below the tunnel were constricted to a smaller area as the velocity of
62
63 685 the impactor was increased, see **Fig. 20(a) – (d)**. The peak positive deformations were observed

686 at the mid location below the tunnel because of the reflected compressive wave from the tunnel
687 boundaries and as the impactor velocity increased the waves got constricted at the middle.

1
2 688

3 689 **6.3 Analytical Evaluation**

4
5 690 The numerical results were compared with the analytical methods available in the
6 literature for the prediction in peak impact force with varying soil cushion depth, see **Fig. 21(a)**.
7 691 The Swiss, Japanese and Australian algorithms didn't have considerations for soil cushion layer
8 692 depth, whereas the Chinese tunnel manual algorithm consider the effect of soil cushion. It was
9 693 observed that the Chinese tunnel manual algorithm predicts the peak impact force much less
10 694 as compared to numerical results. However, all other algorithms have good predictions for peak
11 695 impact force for 0m burial depth and 0.25 and 0.3 m burial depths. The use of numerical
12 696 simulations is further compared with analytical methods for varying impactor mass and
13 697 velocity, see **Fig. 21(b) and (c)**. It was observed that the analytical methods underpredict the
14 698 peak impact force as compared to numerical methods. However, on increasing the mass of the
15 699 impactor, the prediction accuracy improved, and optimum prediction accuracy was observed
16 700 for Yang Qixin's algorithm. The Australian algorithm overpredicts the peak impact force with
17 701 higher impactor velocity. For better prediction, R_c parameter which is described as the
18 702 indentation resistance needs to be calibrated. In the present study, numerical results on varying
19 703 velocities of the impactor, match well with the analytical algorithms. Similar to impactor
20 704 velocity, the Australian algorithm overestimates the peak impact force as compared to other
21 705 methods for higher mass. However, the numerical methods showed similar results compared
22 706 with the other methods and can be used as a benchmark for the design and evaluation of
23 707 concrete tunnels under impact loading.
24
25
26
27
28
29
30
31
32
33
34
35
36
37
38
39

40 709

41 710 **7. Conclusions**

42
43 711 The experimental and numerical investigation on reinforced concrete tunnels was
44 712 performed for varying burial depths of soil cushion layer under low-velocity impact. The
45 713 tunnels were investigated experimentally considering 0.05, 0.1 and 0.15 m of soil cushion
46 714 layer. The numerical study was performed for tunnels under repeated impacts for evaluation of
47 715 the peak force, displacement, and energy absorption capacity of the tunnel. The parametric
48 716 study was performed for the impact resistance and energy absorption of the tunnel for varying
49 717 mass and velocity of the impactor. Based on the study, the following conclusions were drawn:
50
51
52
53
54 718 • The resistance of the tunnel was found to be increasing significantly as the burial depth
55 719 of soil was increased from 0.05 to 0.1 m. The mode of failure was changing with each
56 720 subsequent impact for the 0 and 0.05 m BD tunnel however for 0.1 and 0.15 m the mode

721 of failure was the same till the 5th and 6th impact and after that, the mode of failure was
722 changed to punching shear failure.

1
2 723 • It was concluded that the numerical results were in good agreement with the experimental
3 724 results for peak displacement and strain in rebar. The peak displacement was reduced by
4
5 725 increasing the burial depth of the soil and negligible displacement was observed for a
6
7 726 burial depth of 0.20 m or higher.

8
9 727 • The impulses were found to be independent of soil burial depth. Further, the energy
10
11 728 absorption capacity of the tunnel was found to be increasing with each subsequent impact
12
13 729 for 0, 0.05, 0.1 and 0.15 m tunnel burial depth. For 0.2 m and higher BD, very less energy
14
15 730 absorption was observed in the tunnel because the burial soil absorbed most of the impact
16
17 731 energy.

18 732 • It was observed that the impact force did not have a clear trend for change in the mass of
19
20 733 the impactor. The impulse was increasing with the mass of the impactor indicating higher
21
22 734 plateau forces for a larger mass of the impactor. Further, the energy absorption capacity
23
24 735 was increasing as the mass of impactors increased.

25 736 • The peak force first decreased and then increased significantly as the velocity of the
26
27 737 impactor increased, however, the impulses were increasing with increasing velocity
28
29 738 highlighting that the plateau of impact force was increasing. The energy absorption
30
31 739 capacity of the tunnel also increased significantly as the velocity of the impactor
32
33 740 increases due to the higher force and displacement observed for higher velocities.

34
35 741 • The bed soil deformations were increasing with both impactor mass as well as impactor
36
37 742 velocity. The hogging deformations were observed below the tunnel and were restricted
38
39 743 to the mid location on increasing mass and velocity of the impactor.

40 744 • The numerical simulations agreed with the analytical methods for peak impact under
41
42 745 varying mass and velocity of the impactor. It was observed that Yang Qixin's algorithm
43
44 746 was best among other predicting algorithms when comparing peak impact force with the
45
46 747 numerical result.

47 748 **Acknowledgment**

49 749 This work is part of the research project “Safeguarding civil underground tunnels against
50
51 750 terrorist blast and explosion shocks”. This is a “Royal Society Yusuf Hamied International
52
53 751 Exchange Award” funded by The Yusuf and Farida Hamied Foundation, with contract number
54
55 752 IES\R2\181054. Their contribution is gratefully acknowledged.

56 753 **References**

58 754 [1] Vittorio G, Piergiorgio G, Ashraf M, Shulin X. Mechanized Tunnelling in Urban Areas:
59
60 755 Design Methodology and Construction Control. CRC Press; 2008.

- 756 [2] Degn Eskesen S, Tengborg P, Kampmann J, Holst Veicherts T. Guidelines for tunnelling
757 risk management: International Tunnelling Association, Working Group No. 2. *Tunn
1 758 Undergr Sp Technol* 2004;19:217–37.
- 3 759 [3] Kusakabe O, Takemura J, Takahashi A, Izawa J, Shibayama S. Physical modeling of
4 seismic responses of underground structures. 12th Int. Conf. Int. Assoc. Comput. Methods
5 760 Adv. Geomech., Goa, India, October 1–6: 2008, p. 1459–1474.
- 7 761 [4] He W, Wu Z, Kojima Y, Asakura T. Failure Mechanism of Deformed Concrete Tunnels
8 Subject to Diagonally Concentrated Loads. *Comput Civ Infrastruct Eng* 2009;24:416–31.
- 10 762 [5] Asakura T, Kojima Y. Tunnel maintenance in Japan. *Tunn Undergr Sp Technol*
11 763 2003;18:161–9.
- 12 764 [6] Li Y, Jin X, Lv Z, Dong J, Guo J. Deformation and mechanical characteristics of tunnel
13 765 lining in tunnel intersection between subway station tunnel and construction tunnel. *Tunn
14 766 Undergr Sp Technol* 2016;56:22–33.
- 16 767 [7] Wang Z, Xie Y, Liu H, Feng Z. Analysis on deformation and structural safety of a novel
17 768 concrete-filled steel tube support system in loess tunnel. *Eur J Environ Civ Eng*
18 769 2021;25:39–59.
- 20 770 [8] Mishra S, Rao KS, Gupta NK, Kumar A. Damage to Shallow Tunnels under Static and
21 771 Dynamic Loading. *Procedia Eng* 2017;173:1322–9.
- 22 772 [9] Mishra S, Kumar A, Rao KS, Gupta NK. Experimental and numerical investigation of the
23 773 dynamic response of tunnel in soft rocks. *Structures* 2021;29:2162–73.
- 24 774 [10] Liu W, Chen J, Chen L, Luo Y, Shi Z, Wu Y, Chen J, Chen L. Nonlinear deformation
25 775 behaviors and a new approach for the classification and prediction of large deformation in
26 776 tunnel construction stage : a case study. *Eur J Environ Civ Eng* 2020;0:1–29.
- 27 777 [11] Wang WL, Wang TT, Su JJ, Lin CH, Seng CR, Huang TH. Assessment of damage in
28 778 mountain tunnels due to the Taiwan Chi-Chi Earthquake. *Tunn Undergr Sp Technol*
29 779 2001;16:133–50.
- 30 780 [12] Zhao P, Xie L, Li L, Liu Q, Yuan S. Large-scale rockfall impact experiments on a RC
31 781 rock-shed with a newly proposed cushion layer composed of sand and EPE. *Eng Struct*
32 782 2018;175:386–98.
- 33 783 [13] Hu J, Li S, Li L, Shi S, Zhou Z, Liu H. Field, experimental, and numerical investigation
34 784 of a rockfall above a tunnel portal in southwestern China 2018:1365–82.
- 35 785 [14] Hu J, Li S, Shi S, Zhang J, Xian G. Development and application of a model test system
36 786 for rockfall disaster study on tunnel heading slope. *Environ Earth Sci* 2019;78:391.
- 37 787 [15] Dhamne RR, Mishra S, Kumar A, Rao KS. Deformation behavior of D-Shaped shallow
38 788 tunnels under dynamic loading conditions. *Structures* 2021;33:3973–83.
- 39 789
40 790

- 791 [16] Gahoi A, Zaid M, Mishra S, Rao KS. Numerical analysis of the tunnels subjected to impact
792 loading. 7th Indian rock Conf. (IndoRock2017). Indorock2017, New Delhi: 2017.
- 1
2 793 [17] Mishra S, Zaid M, Rao KS, Gupta NK. FEA of Urban Rock Tunnels Under Impact
3 794 Loading at Targeted Velocity. Geotech Geol Eng 2021.
- 5 795 [18] Rao KS, Sarmah R, Mishra S. Effect of projectile penetration on shallow tunnels. 50th
6 796 Indian Geotech. Conf. 17th-19th December 2015, Pune, Maharashtra: 2015.
- 8 797 [19] Meng G, Gao B, Zhou J, Cao G, Zhang Q. Experimental investigation of the mechanical
9 798 behavior of the steel fiber reinforced concrete tunnel segment. Constr Build Mater
10 799 2016;126:98–107.
- 14 800 [20] Yan Q, Li B, Geng P, Chen C, He C, Yang W. Dynamic response of a double-lined shield
15 801 tunnel to train impact loads. Tunn Undergr Sp Technol 2016;53:33–45.
- 18 802 [21] Sharma H, Mishra S, Rao KS, Gupta NK. Effect of cover depth on deformation in tunnel
19 803 lining when subjected to impact load. ISRM Int. Symp. Asian Rock Mech. Symp.,
20 804 OnePetro: 2018, p. 978–981.
- 23 805 [22] Wang S, Liu Y, Du K, Zhou J. Dynamic Failure Properties of Sandstone Under Radial
24 806 Gradient Stress and Cyclical Impact Loading. Front Earth Sci 2019;7.
- 27 807 [23] Wang H, Guo C, Wang F, Ni P, Sun W. Peridynamics simulation of structural damage
28 808 characteristics in rock sheds under rockfall impact. Comput Geotech 2022;143:104625.
- 31 809 [24] Woods RD. Screening of Surface Wave in Soils. J Soil Mech Found Div 1968;94:951–79.
- 33 810 [25] Abdul Quadir Bhatti NK. A numerical investigation for rock fall impact behaviour of pit
34 811 head of tunnel with falling weight impact loading. 10th Int. Ls-Dyna User Conf., 2008.
- 36 812 [26] Volkwein A, Schellenberg K, Labiouse V, Agliardi F, Berger F, Bourrier F, Dorren LKA,
37 813 Gerber W, Jaboyedoff M. Rockfall characterisation and structural protection – a review.
38 814 Nat Hazards Earth Syst Sci 2011;11:2617–51.
- 41 815 [27] Rezagholilou A, Nikraz H. Protective layer for tunnels under rock fall impacts. Proc.
42 816 World Tunn. Congr. WTC 2013, 2013, p. 1632.
- 45 817 [28] Baziari MH, Shahnazari H, Kazemi M. Mitigation of surface impact loading effects on the
46 818 underground structures with geofam barrier: Centrifuge modeling. Tunn Undergr Sp
47 819 Technol 2018;80:128–42.
- 50 820 [29] Zaid M. Dynamic stability analysis of rock tunnels subjected to impact loading with
51 821 varying UCS. Geomech Eng 2021;24:505–18.
- 54 822 [30] Xu ZH, Wang WY, Lin P, Wang XT, Yu TF. Buffering Effect of Overlying Sand Layer
55 823 Technology for Dealing with Rockfall Disaster in Tunnels and a Case Study. Int J
56 824 Geomech 2020;20:04020127.
- 59 825 [31] Pichler B, Hellmich C, Mang HA. Impact of rocks onto gravel Design and evaluation of

- 826 experiments. *Int J Impact Eng* 2005;31:559–78.
- 827 [32]Dhamne R, Mishra S, Kumar A, Rao KS. Numerical Study of the Cross-Sectional Shape
1 828 of Shallow Tunnels Subjected to Impact and Blast Loading. *Natl. Conf. Prospect. Retrospect.*
2
3 829 *Eng. Geol. Geophys. Instrum. (EGCON 2018)*, 2018.
- 4
5 830 [33]Li Y, Zhang S, Xu J. Experimental research on dynamic model material of high concrete
6
7 831 dam. *Rock Soil Mech* 2011;32:757–61.
- 8
9 832 [34]Liu X, Sheng Q, Chen J, KE W, Yang J. Seismic shaking table test for large-scale
10
11 833 underground cavern group (II): test scheme. *Rock Soil Mech* 2015;36:1683–90.
- 12
13 834 [35]Kutter BL. Dynamic centrifuge modeling of geotechnical structures. *Transp Res Rec*
14
15 835 1992:24–30.
- 16 836 [36]Verma AK, Sardana S, Sharma P, Dinpuia L, Singh TN. Investigation of rockfall-prone
17
18 837 road cut slope near Lengpui Airport, Mizoram, India. *J Rock Mech Geotech Eng*
19
20 838 2019;11:146–58.
- 21
22 839 [37]Stoffel FDSM. Order To Assess the Technical Possibilities of Individual Rockfalls
23
24 840 1998:37–47.
- 25 841 [38]IS: 10262. Concrete Mix Proportioning - Guidelines. Bur Indian Stand New Delhi 2019.
- 26
27 842 [39]IS 456: Code of practice for plain and reinforced concrete. Bureau of Indian Standards,
28
29 843 New Delhi, India; 2000.
- 30
31 844 [40]China PR of. Test methods of concrete and reinforced concrete sewer pipes. Beijing:
32
33 845 People’s Republic of China; 2017.
- 34
35 846 [41]Ni P, Shen L, Mei G, Jiang P. Load Capacity of Perforated Reinforced Concrete Sewer
36
37 847 Pipes. *J Pipeline Syst Eng Pract* 2022;13.
- 38 848 [42]Hrynyk TD, Vecchio FJ. Modeling of reinforced and fiber-reinforced concrete slabs under
39
40 849 impact loads. *Am Concr Institute, ACI Spec Publ* 2017;2017-Janua:118–37.
- 41
42 850 [43]Labieuse V, Descoedres F, Montani S. Experimental Study of Rock Sheds Impacted by
43
44 851 Rock Blocks. *Struct Eng Int* 1996;6:171–6.
- 45 852 [44]Kishi N, Ikeda K, Konno H, Kawase R. Prototype impact test on rockfall retaining walls
46
47 853 and its numerical simulation. *WIT Trans Built Environ* 2000;48.
- 48
49 854 [45]Qixin Y, Baoshu G. Test and research on calculating method of falling stone impulsive
50
51 855 force. *J China Railw Soc* 1996;18:101–6.
- 52
53 856 [46]Luo FJ, Zhou XJ, Wang Y, Zhang FL. Experimental study on rockfall impact force applied
54
55 857 to frame shed tunnels. *J Highw Transp Res Dev (English Ed)* 2018;12:59–66.
- 56 858 [47]Lubliner J, Oliver J, Oller S, Oñate E. A plastic-damage model for concrete. *Int J Solids*
57
58 859 *Struct* 1989;25:299–326.
- 59
60 860 [48]Lee J, Fenves GL. Plastic-Damage Model for Cyclic Loading of Concrete Structures. *J*
61
62
63
64
65

861 Eng Mech 1998;124:892–900.

862 [49] Gupta I. Experimental and Numerical Studies on the Resilience capacity of the Reinforced
1 863 Concrete Tunnel Against Free-Fall Impact Loading. Dissertation of Master of Technology,
2 864 Submitted to Dr B R Ambedkar NIT Jalandhar, Punjab, 2019.

5 865 [50] Zaid M. Preliminary Study to Understand the Effect of Impact Loading and Rock
6 866 Weathering in Tunnel Constructed in Quartzite. Geotech Geol Eng 2021.

8 867 [51] Hafezolghorani M, Hejazi F, Vaghei R, Jaafar MS Bin, Karimzade K. Simplified Damage
9 868 Plasticity Model for Concrete. Struct Eng Int 2017;27:68–78.

11 869 [52] Johnson GR, Cook WH. Fracture characteristics of three metals subjected to various
12 870 strains, strain rates, temperatures and pressures. Eng Fract Mech 1985;21:31–48.

14 871 [53] Iqbal MA, Rai S, Sadique MR, Bhargava P. Numerical simulation of aircraft crash on
15 872 nuclear containment structure. Nucl Eng Des 2012;243:321–35.

17 873 [54] Kumar V, Kartik KV, Iqbal MA. Experimental and numerical investigation of reinforced
18 874 concrete slabs under blast loading. Eng Struct 2020;206:110125.

20 875 [55] DS Simulia Corp. ABAQUS/CAE User's Guide, Dassault Systèmes (DS) Simulia Corp.
21 876 RI, USA: 2019.

23 877 [56] Kim D-J, Youn J-U, Jee S-H, Choi J, Lee J-S, Kim D-S. Numerical Studies on Bearing
24 878 Capacity Factor N_γ and Shape Factor of Strip and Circular Footings on Sand According
25 879 to Dilatancy Angle. J Korean Geotech Soc 2014;30:49–63.

27 880 [57] Meyerhof GG. Some Recent Research on the Bearing Capacity of Foundations. Can
28 881 Geotech J 1963;1:16–26.

30 882 [58] Maranha JR. The experimental determination of the angle of dilatancy in soils. Geotech
31 883 Eng 2009;147–50.

33 884 [59] Zhou J, Wen P, Wang S. Numerical investigation on the repeated low-velocity impact
34 885 behavior of composite laminates. Compos Part B Eng 2020;185:107771.

36 886

37 887

38 888

39

40

41

42

43

44

45

46

47

48

49

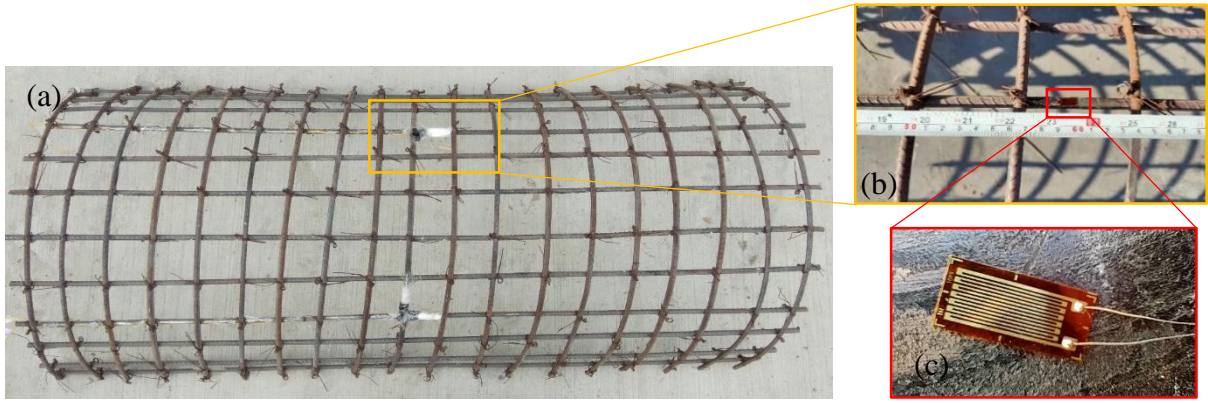


Fig. 1. Typical illustrations of (a) RC tunnel (b) location of strain gauge and (c) strain gauge



Fig. 2. Experimental setup of (a) bare tunnel (b) tunnel with soil cushion layer and (c) drop weight impactor

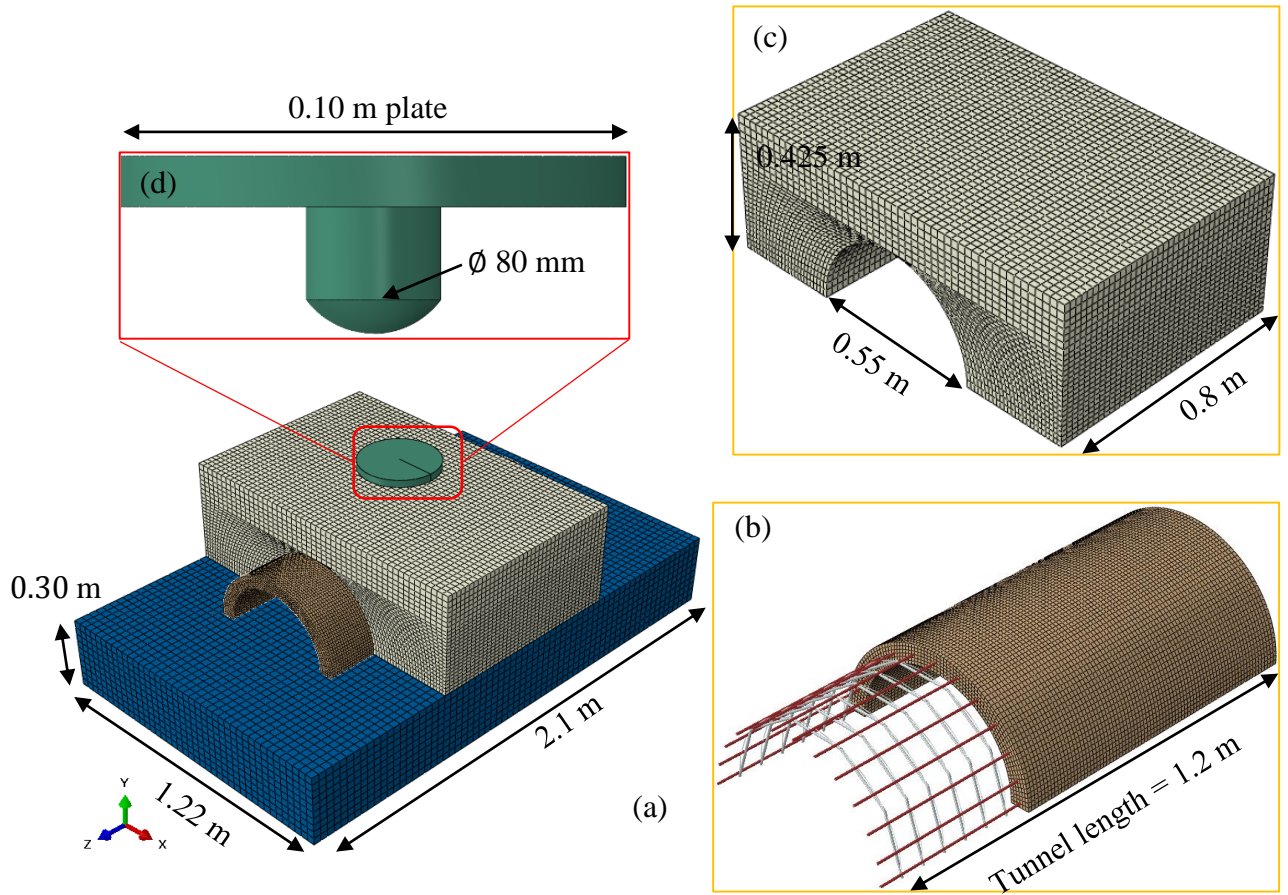


Fig. 3. (a) Assembly of the model (b) embedded rebar (c) burial soil and (d) rigid impactor

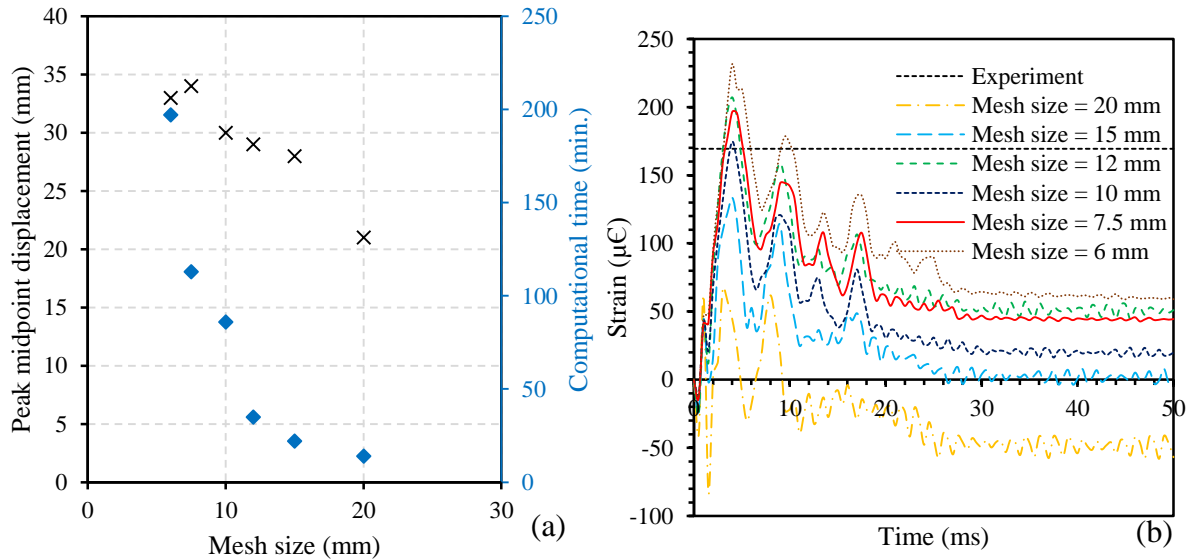


Fig. 4. (a) Mesh convergence study on tunnel and (b) prediction of strain in reinforcement for T-1-BD0

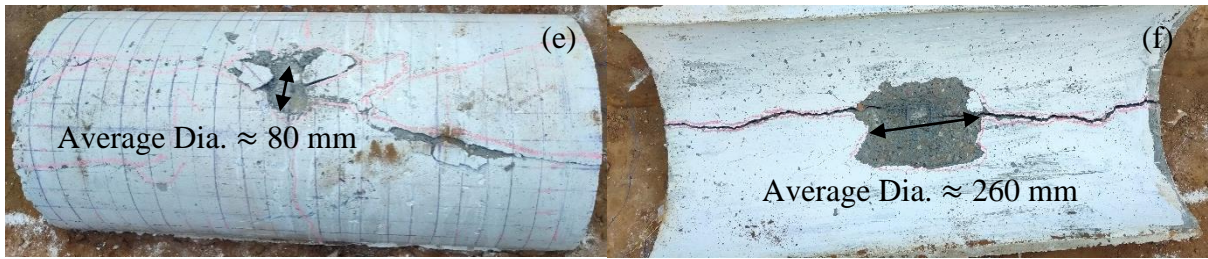
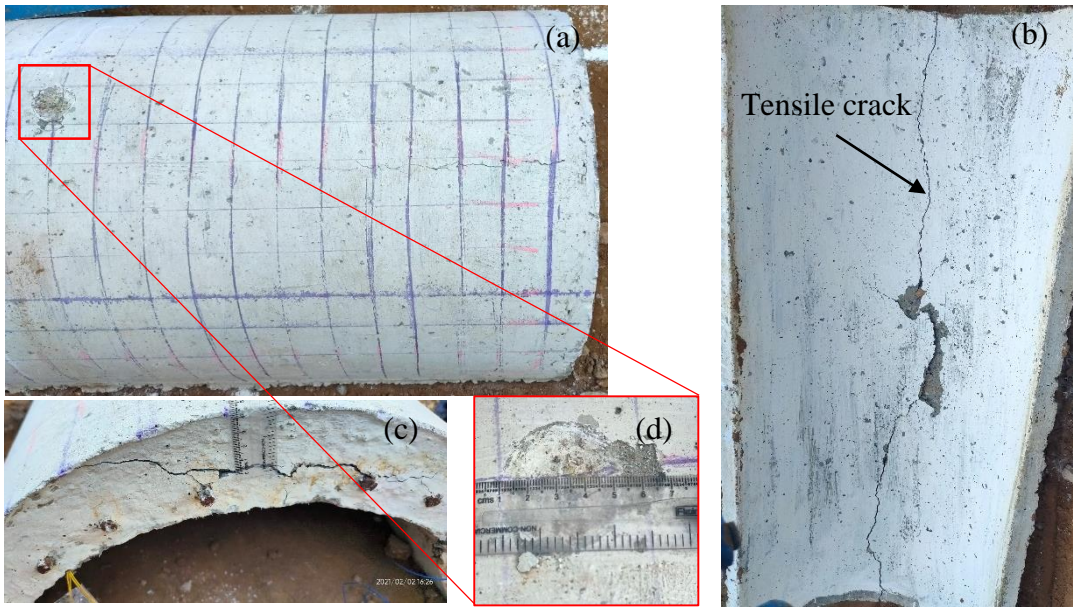


Fig. 5. Damage to specimen T-1-BD0 at 1st impact for (a) front, (b) rear, (c) side face, (d) front crater and for 2nd impact at (e) front face and (f) rear face

1
2
3
4
5
6
7
8
9
10
11
12
13
14
15
16
17
18
19
20
21
22
23
24
25
26 911
27 912
28
29 913
30
31 914
32
33 915
34
35 916
36
37 917
38
39 918
40 919
41
42 920
43
44 921
45
46 922
47
48 923
49 924
50
51 925
52
53 926
54
55 927
56
57 928
58
59 929
60 930
61
62
63
64
65

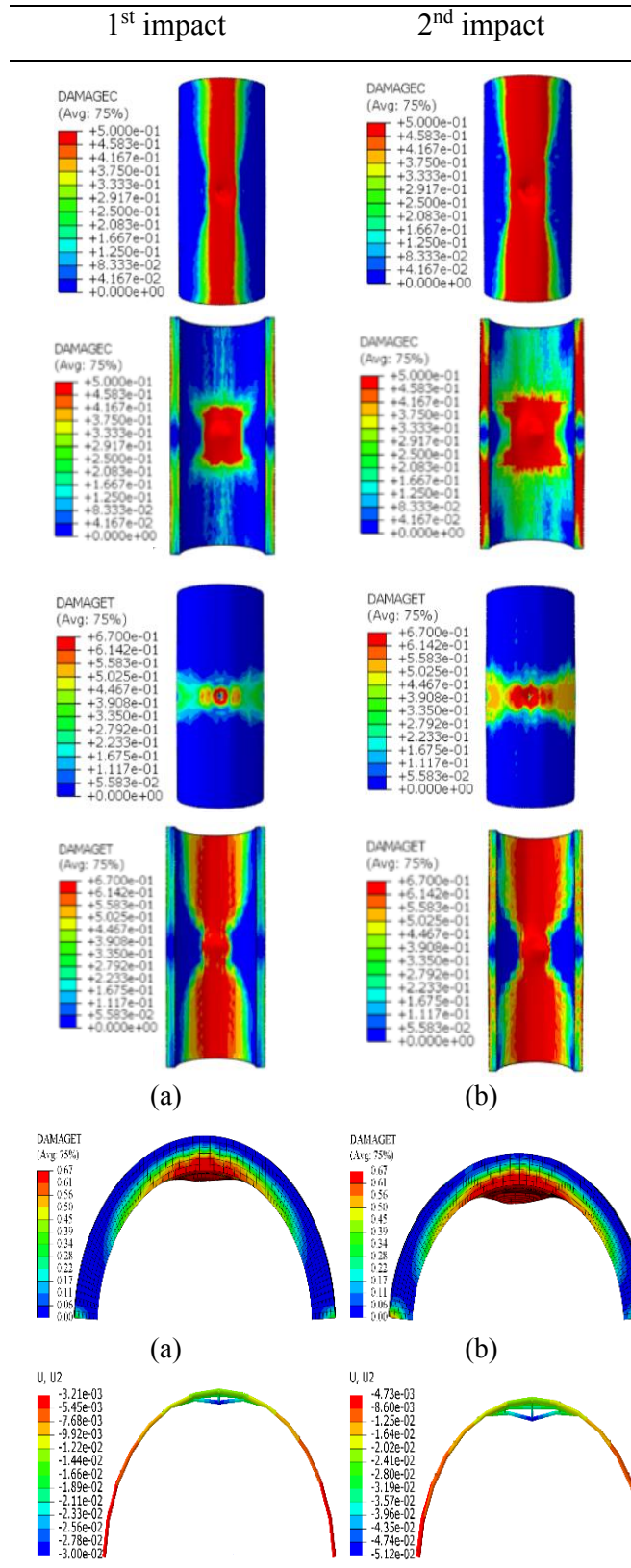


Fig. 6. Compression and tension damage to the tunnel T-1-BD0 at front and rear face under repeated impacts (a) side face and (b) displacement in rebar

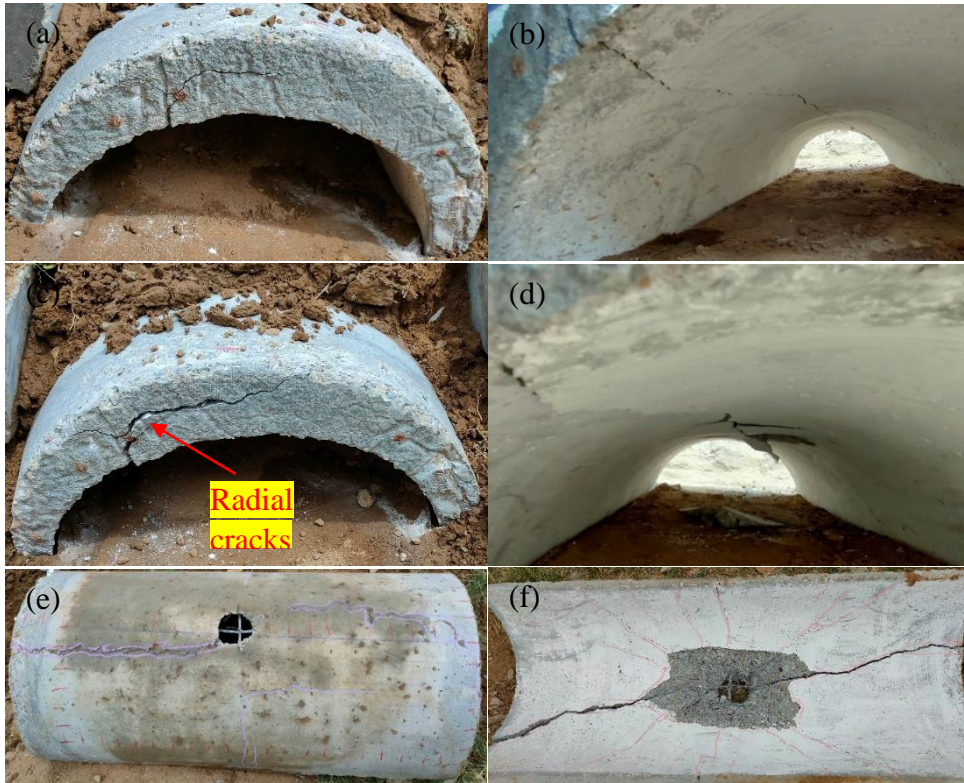


Fig. 7. Damage to the tunnel T-2-BD5 under (a), (b) 1st impact (c), (d) 2nd impact and (e), (f) 3rd impact

1
2
3
4
5
6
7
8
9
10
11
12
13
14
15
16
17
18
19
20
21
22
23 937
24 938
25
26 939
27
28 940
29
30 941
31
32 942
33 943
34
35 944
36
37 945
38
39 946
40
41 947
42 948
43
44 949
45
46 950
47
48 951
49
50 952
51
52 953
53 954
54
55 955
56
57 956
58
59 957
60
61
62
63
64
65

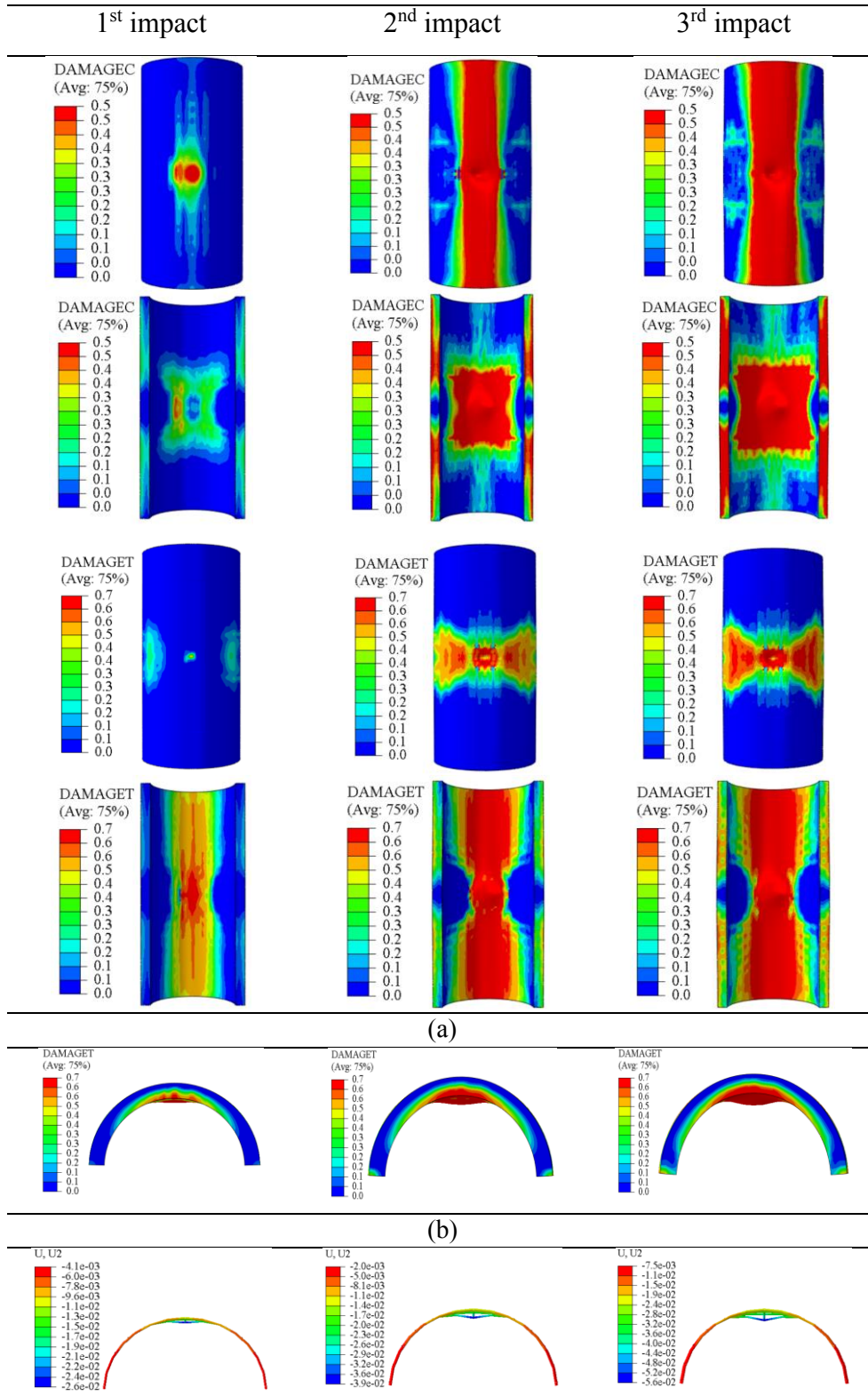


Fig. 8. Compression and tension damage to the tunnel T-2-BD5 at front and rear face under repeated impacts (a) side face and (b) displacement in rebar



Fig. 9. Damage to tunnel side face (a-e) 1st impact to 5th impact, (f-i) 6th impact, (g) damage to soil cushion layer for 6th impact, (h-i) damage to side face for 7th impact (j) damage to damage to soil cushion layer for 7th impact and (k) & (l) front and rear face damage on 8th impact

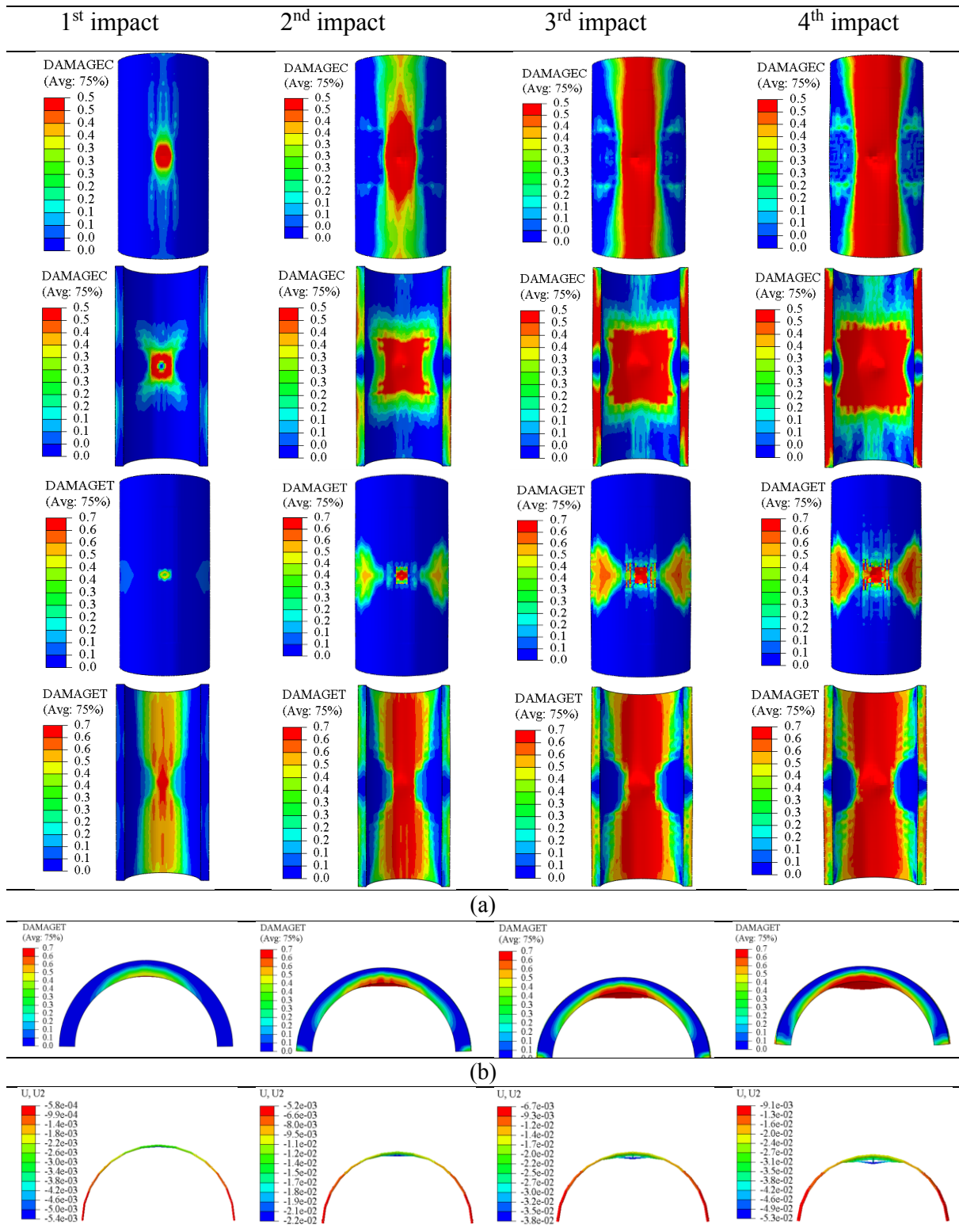


Fig. 10. Compression and tension damage to the tunnel T-3-BD10 at front and rear face under repeated impacts (a) rear face and (b) displacement in rebar

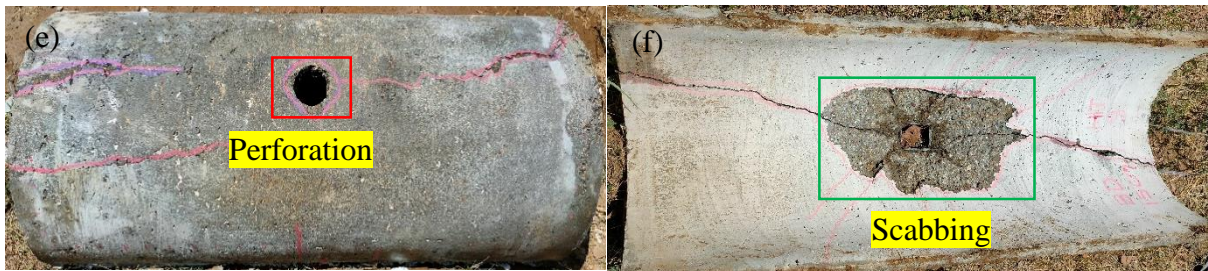
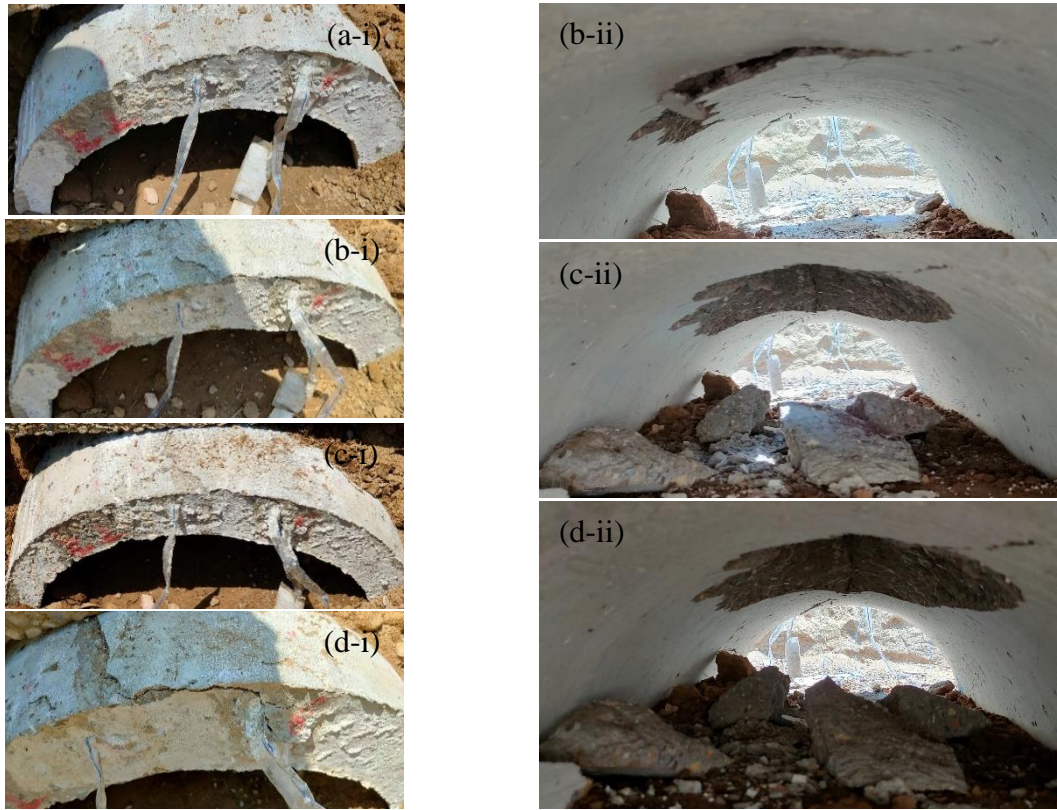


Fig. 11. Damage to the tunnel T-4-BD15 (i) side face and (ii) rear face for impact (a) 5th (b) 6th (c) 7th (d) 8th and final failure at 9th impact for (e) front and (f) rear face

1
2
3
4
5
6
7
8
9
10
11
12
13
14
15
16
17
18
19
20
21
22
23
24
25
26
27
28
29
30
31
32 986
33
34 987
35 988
36 989
37 990
38 991
39 992
40 993
41 994
42 995
43 996
44 997
45 998
46 999
47 1000
48 1001
49 1002
50 1003
51 1004
52 1005
53 1006
54 1007
55 1008
56
57
58
59
60

61
62
63
64
65

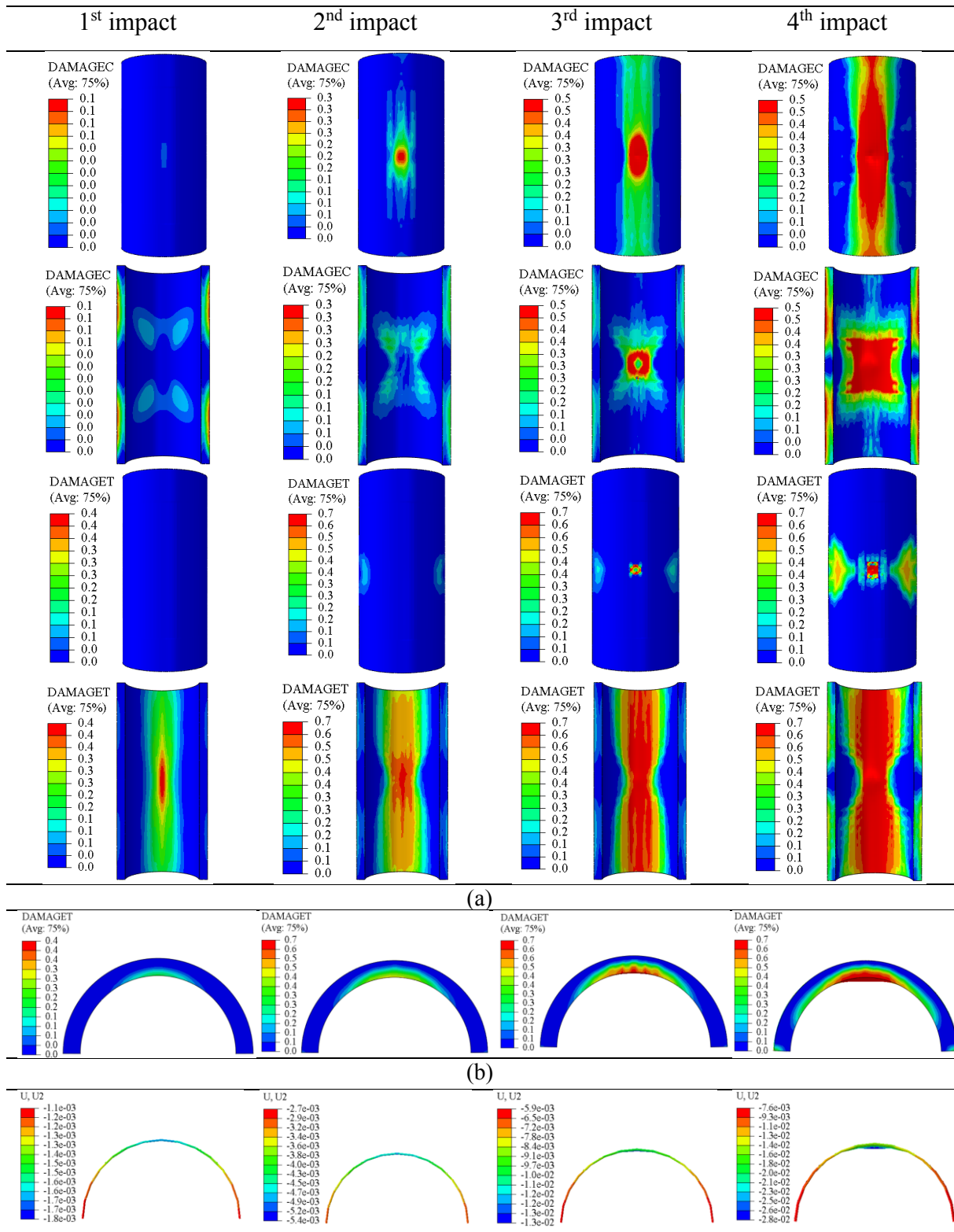


Fig. 12. Compression and tension damage to the tunnel T-4-BD15 at front and rear face under repeated impacts (a) side face and (b) displacement in rebar

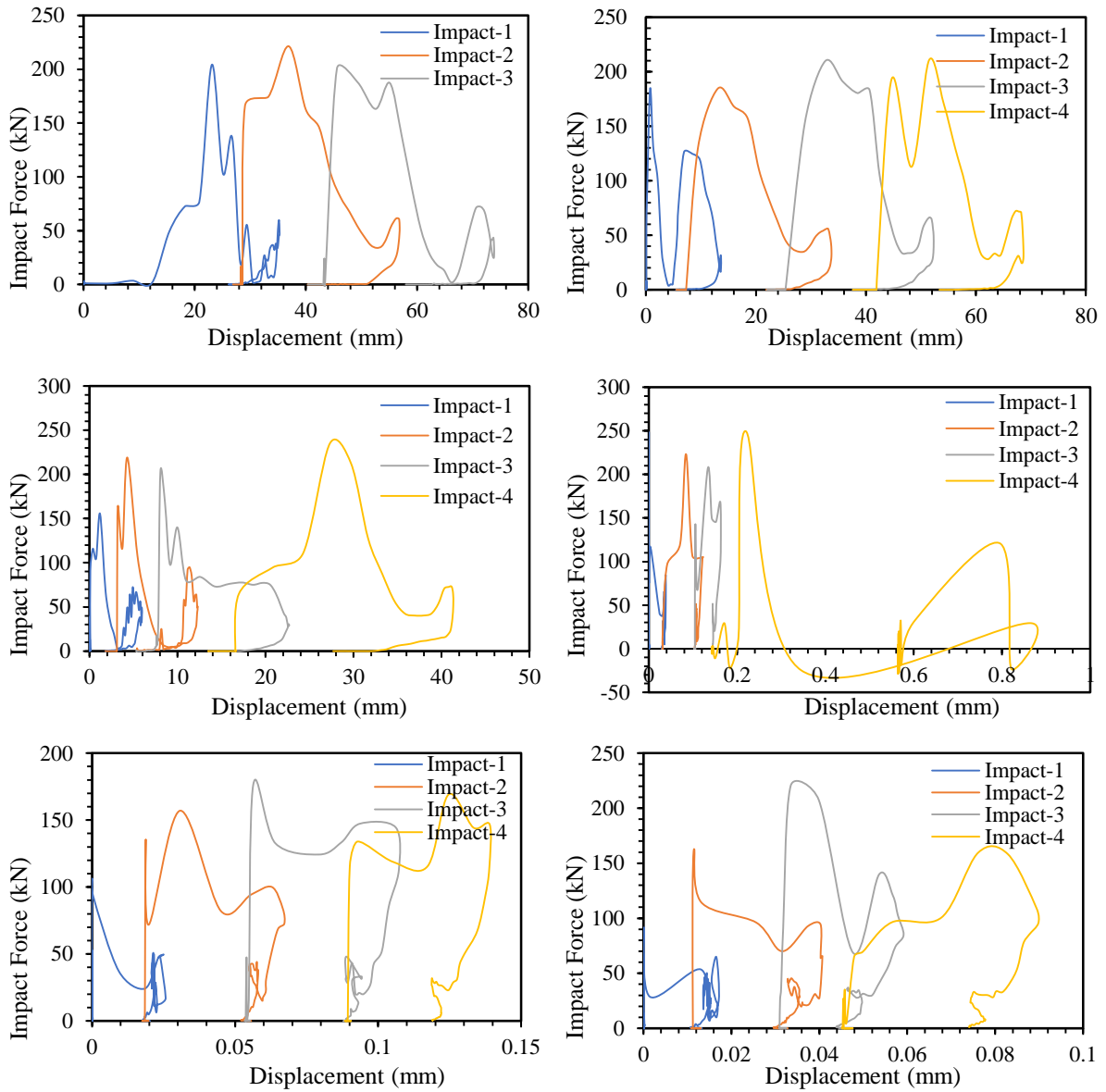


Fig. 13. Impact force-displacement curves under repeated impacts for varying burial depths of (a) 0.05 (b) 0.10 (c) 0.15 (d) 0.20 (e) 0.25 and (f) 0.30 m

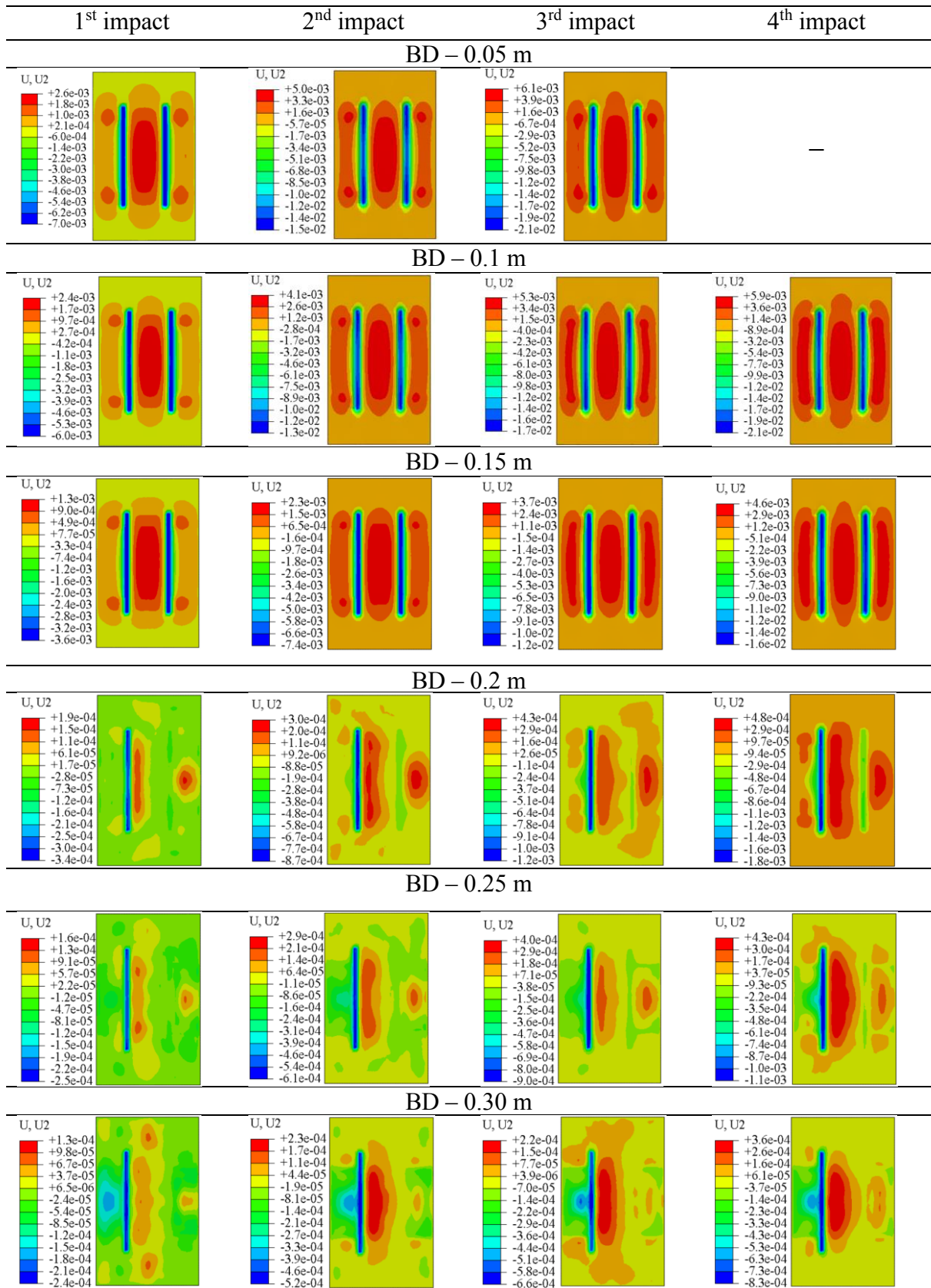


Fig. 14. Deformation in bed soil with respect to initial position for different burial depths under 1st, 2nd, 3rd, and 4th impact respectively

1
2
3
4
5
6
7
8
9
10
11
12
13
14
15
16
17
18
19
20
21
22
23
24
25
26
27
28
29
30
31
32
33
34
35
36
37
38
39
40
41
42
43
44
45
46
47
48
49
50
51
52
53
54
55
56
57
58
59
60
61
62
63
64
65

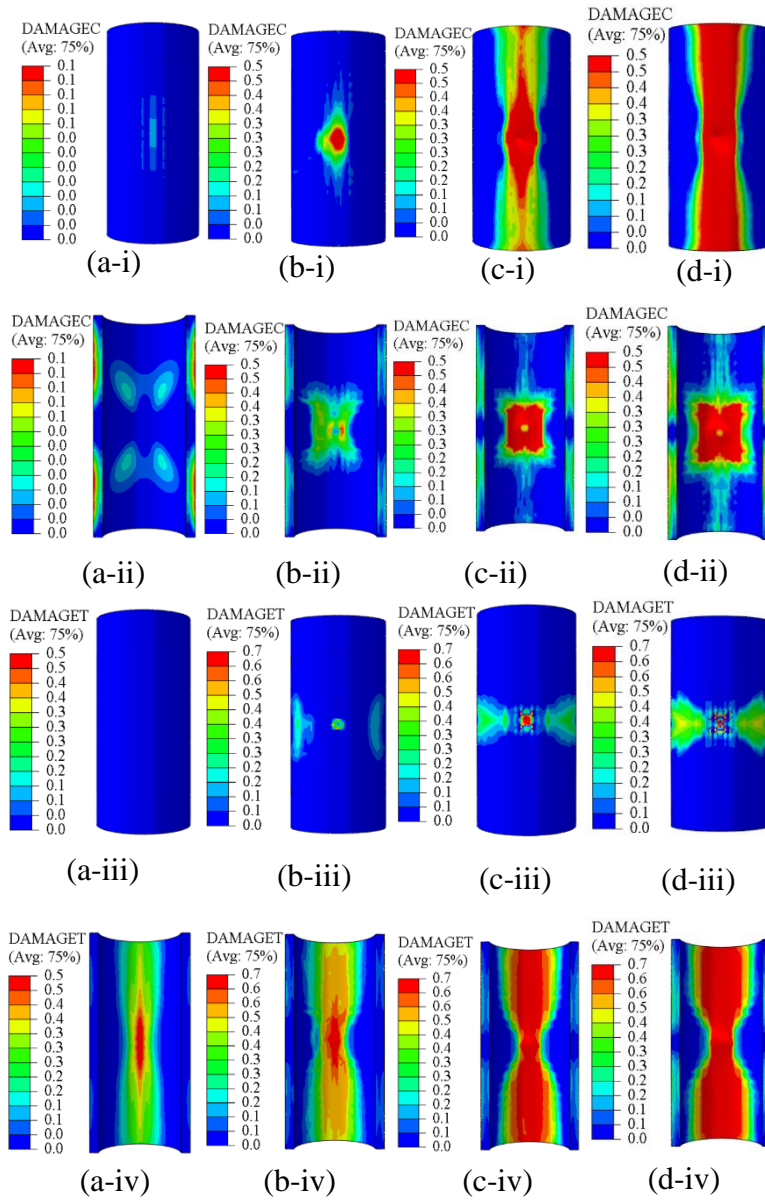


Fig. 15. (i) Front face, (ii) rear face compression damage (iii) front face and (iv) rear face tension damage for impactor mass of (a) 150 (b) 200 (c) 300 and (d) 400 kg

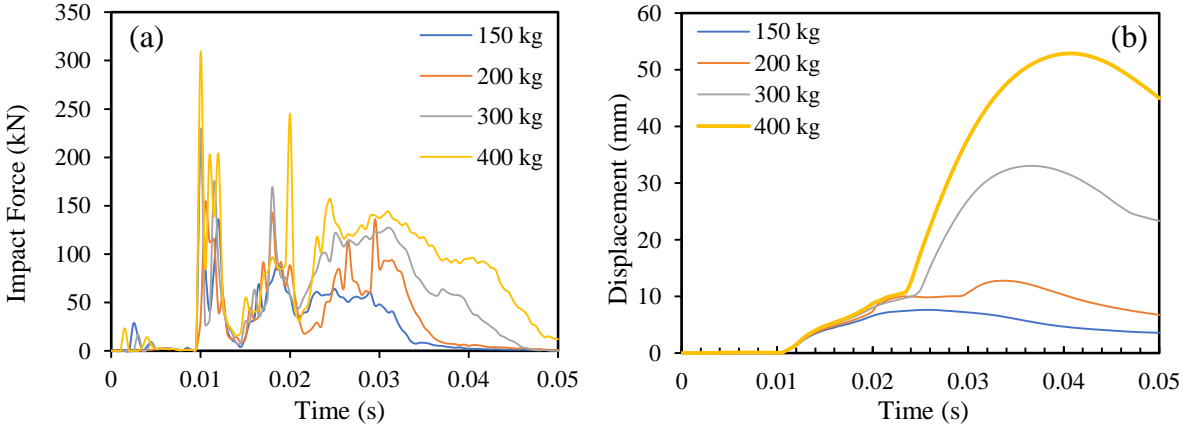


Fig. 16. (a) impact force and (b) displacement with varying mass of impactor

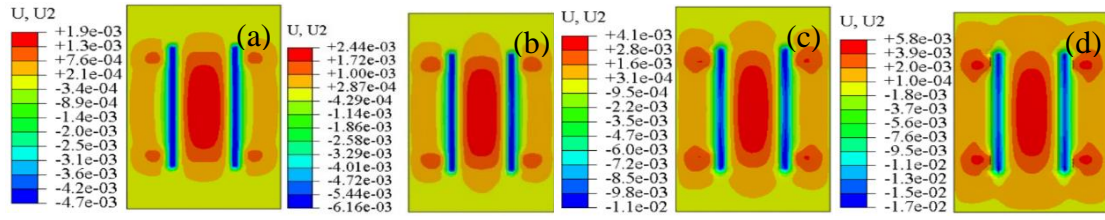


Fig. 17. Deformation (m) in soil against (a) 150 (b) 200 (c) 300 and (d) 400 kg mass impactor

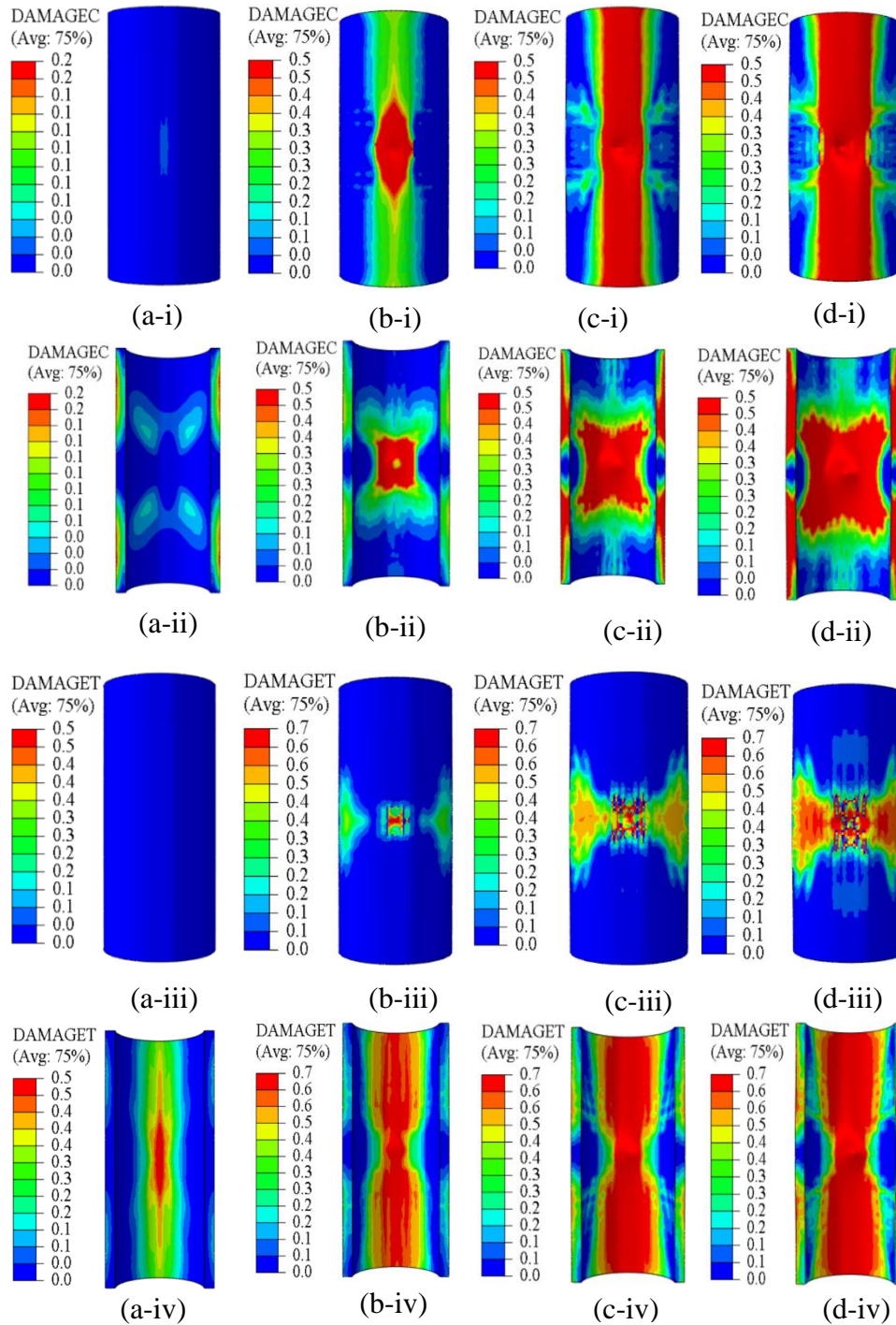


Fig. 18. (i) Front face and (ii) rear face compression damage (iii) front face and (iv) rear face tension damage under velocity of (a) 9.9 (b) 14 (c) 17.15 and (d) 19.81 ms^{-1}

1048
1049

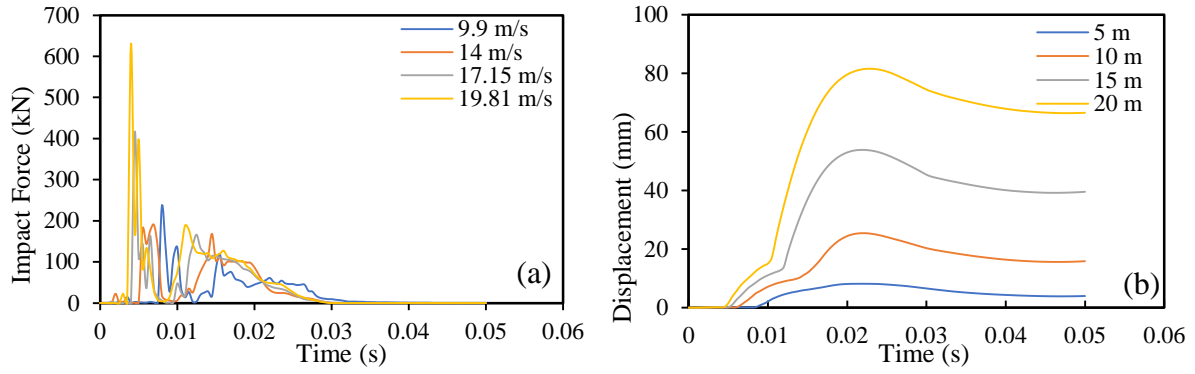


Fig. 19. Variation of (a) impact force and (b) displacement of tunnel with varying velocity of impactor

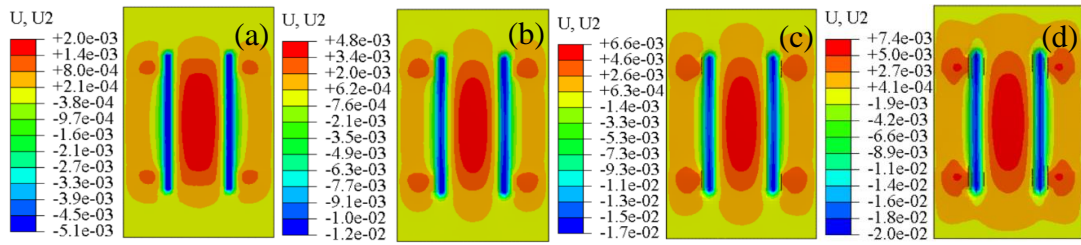
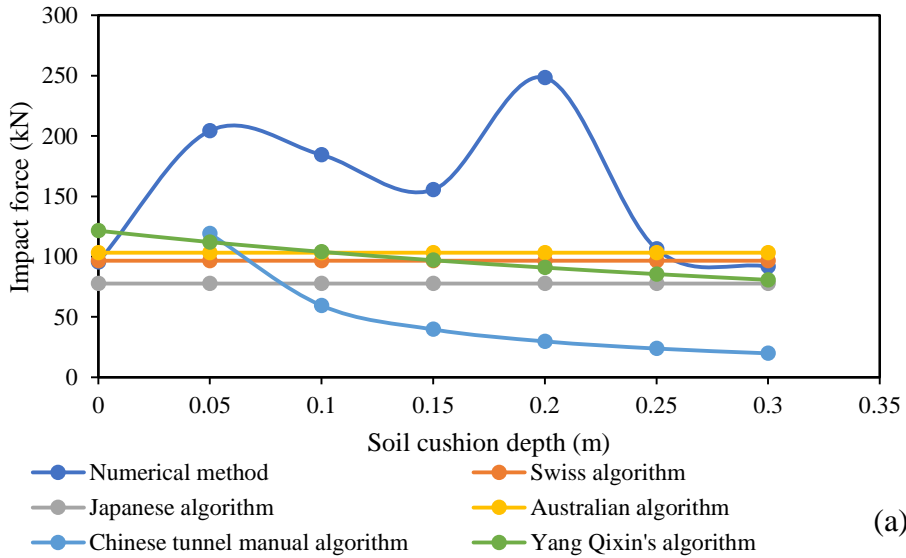


Fig. 20. Deformation in soil bed for impactor velocity (a) 9.9 (b) 14 (c) 17.15 and (d) 19.81 ms⁻¹



(a)

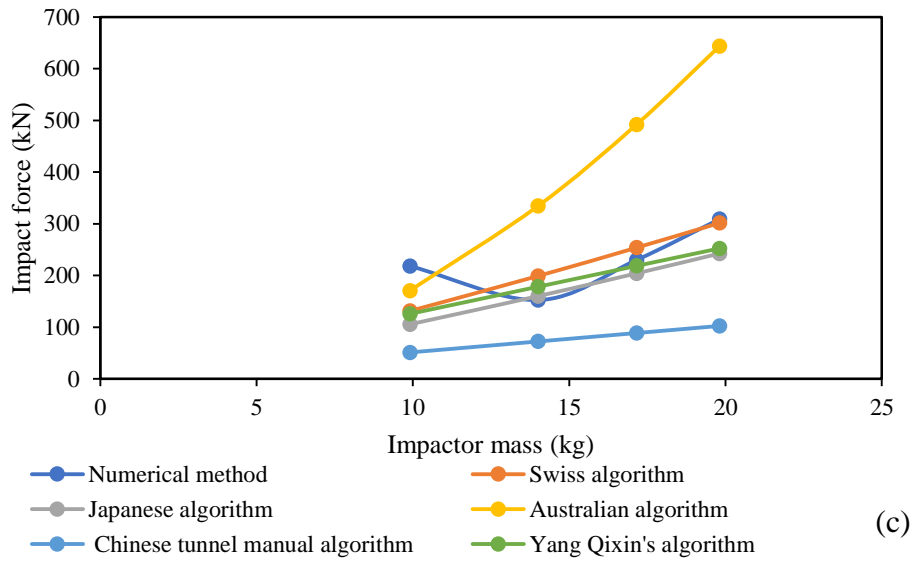
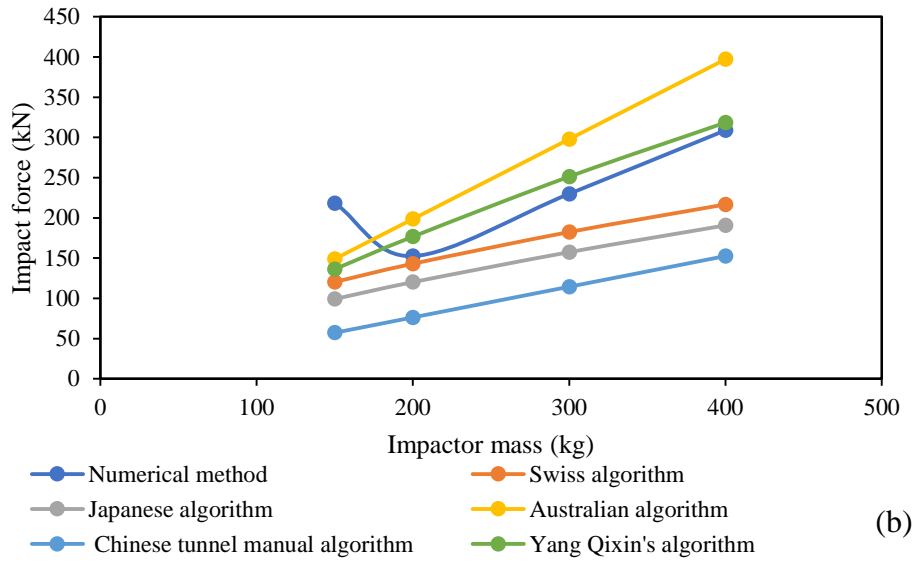


Fig. 21 Comparison of analytical methods with numerical simulation for varying (a) soil cushion depth (b) impactor mass and (c) impactor velocity

1078

1079

Table 1. The law of similitude [34]

Parameter	Scale factor	Parameter	Scale factor
Length	δ	Mass	δ^3
Velocity	$\sqrt{\delta}$	Stress	1
Time	δ	Strain	1
Energy	δ^4	Elastic modulus	1
Acceleration	δ	Force	δ^2

91080

10

111081

12

131082

Table 2 Details of experimental program

Nomenclature	Burial Depth, m	Impact velocity, m/s	Impact momentum, kg.m/s	Impact Energy, J
T-1-BD0	0	7.67	797.68	3060.72
T-2-BD5	0.05	7.67	797.68	3060.72
T-3-BD10	0.10	7.67	797.68	3060.72
T-4-BD15	0.15	7.67	797.68	3060.72

211083

22

231084

24

25

26

27

28

29

30

31

32

33

34

35

36

37

38

391085

40

411086

42

431087

44

451088

46

471089

48

491090

50

511091

52

531092

54

551093

56

571094

58

591095

60

611096

62

63

64

65

Table 3 Multi-axial behaviour of CDP model [49]

Parameter	Value
Density, ρ (kg/m ³)	2400
Young's Modulus, E (N/m ²)	24×10^9
Poisson's ratio, μ	0.15
Dilation angle	30°
Eccentricity, m	0.1
K	0.66
f_{b0}/f_{c0}	1.16

Table 4 Uni-axial compressive and tensile behavior of CDP model [49]

Yield stress (N/m ²) × 10 ⁶	Inelastic strain (m/m)	Damage parameter
Compressive behavior		
21	0	0
20	0.0011	0.20
19	0.0040	0.50
Tensile behavior		
3.3	0	0
3.2	0.003	0.50
3.1	0.005	0.55
3	0.007	0.61
2.9	0.010	0.67

1099

1100

Table 5 Johnson-cook model parameters for steel Fe 415 [53,54]

Description	Parameters
Density, ρ (kg/m ³)	7850
Young's Modulus, E (N/m ²)	200×10^9
Poisson's ratio, μ	0.33
Yield stress constant, A (N/m ²)	493×10^6
Strain hardening constant, B (N/m ²)	383×10^6
n	0.45
Viscous effect, C	0.0114
Thermal softening constant, m	0.94
Reference strain rate, $\dot{\epsilon}$	0.0005
Melting temperature (K)	1800
Transition temperature (K)	293
Fracture strain Constant	
D_1	0.0705
D_2	1.732
D_3	-0.54
D_4	-0.015
D_5	0

1101

1102

1103

Table 6 Material constant for soil [49, 56-57]

Density (kg/m ³)	Elastic modulus (N/m ²)	Poisson ratio	Dilatation angle (°)	Angle of internal friction (°)	Flow stress ratio
1850	20.9×10^6	0.36	1	31	0.778

1104

1105

1106

1107 **Table 7** Summary of Numerical study of tunnel under various burial depths for repeated

1108 impacts

Case	Peak force (kN)	Peak displacement in tunnel (mm)	Impulse (kN-s)	Energy absorption capacity of tunnel (kN-mm)	Peak bed soil deformation w.r.t. base position (mm)
0 m Burial Depth					
Impact 1	95.55	46.48	0.85	2998.62	-18.35
Impact 2	110.38	79.34	0.91	2912.05	-39.6
0.05 m Burial Depth					
Impact 1	204.32	35.27	0.93	1430.92	-7
Impact 2	221.41	56.87	0.98	3326.07	-15
Impact 3	200.65	73.88	0.93	3013.83	-21
0.10 m Burial Depth					
Impact 1	184.34	13.67	0.90	1077.49	-6
Impact 2	184.21	33.73	0.85	2574.60	-13
Impact 3	209.6	52.31	0.94	3178.30	-17
Impact 4	210.54	68.65	0.89	2810.96	-21
0.15 m Burial Depth					
Impact 1	155.43	5.96	0.96	316.28	-3.60
Impact 2	219.08	12.27	0.96	583.86	-7.40
Impact 3	202.63	22.67	0.88	1230.62	-12
Impact 4	234.76	41.33	0.87	2587.04	-16
0.20 m Burial Depth					
Impact 1	248.36	0.04	0.89	2.55	-0.34
Impact 2	223.26	0.12	0.81	10.27	-0.87
Impact 3	206.48	0.16	0.93	7.53	-1.20
Impact 4	249.56	0.86	0.17	0.58	-1.80
0.25 m Burial Depth					
Impact 1	106.36	0.03	0.86	1.09	-0.25
Impact 2	157.01	0.07	0.88	4.67	-0.61
Impact 3	176.06	0.11	0.88	6.41	-0.90
Impact 4	169.06	0.14	0.87	5.63	-1.10
0.30 m Burial Depth					
Impact 1	91.73	0.02	0.82	0.57	-0.24
Impact 2	162.87	0.04	0.91	2.67	-0.52
Impact 3	220.53	0.06	1.01	3.50	-0.66
Impact 4	159.44	0.09	0.83	4.20	-0.83

1109
1110
1111
1112 **Table 8** Parametric analysis for varying mass of impactor

Case kg	Peak force (kN)	Peak displacement in tunnel (mm)	Impulse (kN-s)	Energy absorption capacity of tunnel (kN-mm)	Peak bed soil deformation w.r.t. base position (mm)
150	218.32	7.63	1.35	346.71	-4.7
200	152.50	12.77	1.66	780.82	-6.1
300	229.88	33.04	2.60	3027.69	-11
400	308.90	52.88	3.77	5742.01	-17

1114

1115

11116

Table 9 Parametric analysis for varying velocity of impactor

Case ms ⁻¹	Peak force (kN)	Peak displacement in tunnel (mm)	Impulse (kN-s)	Energy absorption capacity of tunnel (kN-mm)	Peak bed soil deformation w.r.t. base position (mm)
9.9	235.21	8.17	1.18	414.10	-5.1
14	189.33	25.45	1.50	2172.16	-12
17.15	416.32	53.88	1.70	5372.27	-17
19.81	630.14	81.59	2.30	9922.37	-20

101117

11

121118

13

141119

15

161120

17

181121

19

201122

21

221123

23

241124

25

261125

27

281126

29

301127

31

321128

33

341129

35

361130

37

381131

39

401132

41

421133

43

441134

45

461135

47

481136

49

501137

51

521138

53

541139

55

561140

57

581141

59

601142

61

621143

63

641144

65

1145 **Highlights**

- 1146 • Influence of cushions on behavior of reinforced concrete tunnels studied under drop impact
1 1147 load.
- 3 1148 • The resistance of tunnel increased with an increase of cushion depth from 0 to 0.10 m.
- 5 1149 • The energy absorption capacity increased from 7.8 to 48.7% against impactor energy from
7 1150 4.41 to 11.77 kJ.
- 9 1151 • The energy absorption in tunnels is more sensitive to mass of impactor as compared to
10 drop height.
- 11 1152
- 12 131153 • Numerical results compared with analytical methods for evaluating peak impact force and
14 similar pattern was observed.
- 15 1154

16
17 1155
18
19 1156
20
21 1157
22
23 1158
24
25 1159

26
27
28
29
30
31
32
33
34
35
36
37
38
39
40
41
42
43
44
45
46
47
48
49
50
51
52
53
54
55
56
57
58
59
60
61
62
63
64
65